TITLE

Human iPSC Models of Ganglioside Deficiency Reveal a Sialylated Lipid Requirement for Plasma-Membrane Organization and Neuronal Activity

AUTHORS

Henry G. Barrow*[,1], Zhuang Z. Han*[,1], Alex S. Nicholson[1], Sinéad Strasser[1], Daniel A. Nash[2], John O. Suberu[1], Robin Antrobus[1], Danielle te Vruchte[3], David A. Priestman[3], Stephen C. Graham [2], Frances M. Platt[3] and Janet E. Deane[1^]

AFFILIATIONS

[1] Cambridge Institute for Medical Research, University of Cambridge, UK

[2] Department of Pathology, University of Cambridge, UK

[3] Department of Pharmacology, University of Oxford, UK

* Equal first authors

^ Corresponding author, jed55@cam.ac.uk

ABSTRACT

Gangliosides are abundant neuronal glycosphingolipids (GSL) whose precise roles in human neuronal function remain poorly defined. Loss of the ganglioside biosynthetic enzymes ST3GAL5 or B4GALNT1 causes severe neurodevelopmental disorders. Using isogenic human iPSC derived cortical neurons, we demonstrated that disruptions of either gene eliminated major neuronal gangliosides yet produced strikingly divergent phenotypic outcomes. ST3GAL5 loss reprogrammed the GSL repertoire, generating non-neuronal globo- and o-series lipids, and abolished network-level electrical activity. In contrast, B4GALNT1 deficient neurons retained almost normal electrical activity, supported by an accumulation of simple sialylated precursor GSLs (GM3/GD3). Proteomic profiling revealed that ST3GAL5 deficiency caused a severe reduction in plasma membrane (PM) protein abundance, including ion channels, GPCRs, and synaptic organizer proteins, while B4GALNT1 loss did not induce PM changes. These findings demonstrate that sialylated GSLs are essential scaffolds for PM organization and neuronal excitability, establishing a mechanistic basis for the severe phenotype caused by loss of the GM3 synthase ST3GAL5 and highlighting key species-specific features of human GSL metabolism.

INTRODUCTION

Glycosphingolipids (GSLs) are essential bioactive lipids that are enriched on the cell surface where they play essential roles in cell recognition, cell identity and membrane protein function[1–3]. GSLs are characterized by structurally diverse glycan headgroups (**Fig.1A**) and interact with cholesterol to form highly ordered membrane microdomains (also known as lipid rafts). These microdomains support the spatial organization and assembly of signalling and adhesion complexes. Although GSLs are also known to be critical players in membrane protein trafficking, the details of how they regulate this process remain unclear[4,5].

Biosynthesis of GSLs involves multiple enzymes that function in a stepwise process to build glycan headgroups onto the ceramide backbone. Gangliosides are a subclass of GSLs containing sialic acid moieties and are particularly important in brain development and function. Two "gatekeeper" enzymes involved in the early steps of ganglioside synthesis are ST3GAL5 (GM3 synthase) and B4GALNT1 (GM2 synthase) with loss-of-function mutations causing severe childhood epilepsy[6] and an early-onset spastic paraplegia[7], respectively. Loss of either enzyme would remove all four predominant neuronal gangliosides (GM1a, GD1a, GD1b and GT1b, **Fig.1B**), but clinical severity differs in these diseases.

GM3 synthase deficiency (GM3SD) is an ultra-rare, autosomal recessive inherited metabolic disorder first characterized in the Old Order Amish community[6], where it was historically known as Amish Infantile Epilepsy Syndrome. However, it has been identified in several additional populations[8–10]. The clinical manifestation of GM3SD typically follows a severe and progressive course: while newborns often appear healthy, they rapidly develop refractory infantile-onset epilepsy, profound intellectual disability, and developmental stagnation within the first months of life[11]. Among the clinically validated pathogenic ST3GAL5 mutations[12], five have been evaluated for residual enzymatic activity. Activity assays conducted in HEK293T cells demonstrate that the most frequently reported variants (G342S, R288X, C195S, G201A and E355K) exhibit a complete lack of detectable enzymatic activity[13].

Hereditary spastic paraplegia 26 (HSP26) is another rare autosomal recessive neurological disorder of GSL synthesis caused by mutations in B4GALNT1. Clinically, HSP26 is distinguished from GM3SD by a later age of onset and a different progression: symptoms typically emerge in late childhood or adolescence as progressive lower-limb spasticity and weakness, sometimes accompanied by cognitive impairment and peripheral neuropathies[14–16]. Enzymatic activity assays demonstrate that the pathogenic B4GALNT1 variant D433A exhibits no detectable

activity[15], whereas other variants of unknown significance display a range of activities from undetectable to near-wildtype levels[15,17].

Murine models have been developed to investigate GM3SD and HSP26, yet both illustrate the limitations of cross-species modelling of GSL disorders. ST3GAL5 knockout mice exhibit informative phenotypes including metabolic alterations[18], peripheral neuropathies[19] and impaired spatial memory[20]. However, they do not reproduce the defining clinical features of GM3SD, notably neurodevelopmental arrest and early-onset epilepsy. In contrast, B4GALNT1 knockout mice display clearer nervous system pathologies, including axonal degeneration and myelination defects[21] and develop progressive motor dysfunction with reflex, strength, coordination and gait abnormalities[22]. Nevertheless, across both disorders, mouse models do not consistently capture the full spectrum and timing of human disease, consistent with prior observations that species differences in GSL metabolism can influence neurological phenotypes[23]. Existing human-based models, such as patient-derived fibroblasts[24] and ST3GAL5 knockout HEK293 cells[25], are limited by their distinct cellular lineages resulting in lipid compositions that do not accurately reflect the neuronal tissue, making them less effective for functional investigations. Human-based neuronal models are therefore essential to understand the pathogenic mechanisms of GSL-related disorders.

Human iPSC-derived neurons offer an excellent isogenic inducible model to study the biochemical and electrophysiological changes when GSL metabolism is disturbed. Mature cortical glutamatergic neurons can be generated within 14 days following doxycycline-induced NGN2 expression, and they acquire functional maturity, including synchronized electrical activity, by day 28[26–28]. This i3N system has been successfully used to investigate molecular mechanisms driving several neurodevelopmental diseases including early onset gangliosidoses[28–30].

Here we set out to define how specific ganglioside repertoires support human neuronal function. We generated i3N models of GM3SD and HSP26 by knocking down the expression of genes *ST3GAL5* or *B4GALNT1*, respectively. Both models lose the predominant neuronal gangliosides, yet only GM3SD neurons fail to develop coordinated network activity, whereas HSP26 neurons maintain normal firing. Proteomic profiling of the plasma membrane reveals a mechanistic basis for this defect, with GM3SD neurons exhibiting significant loss of surface ion channels, GPCRs, and synaptic adhesion molecules, while the HSP26 membrane proteome remains largely intact. Together, these findings provide a mechanistic explanation for the distinct cellular and clinical

phenotypes of GM3SD and HSP26, establishing a framework for dissecting how sialylated versus non sialylated GSLs shape neuronal maturation and function.

RESULTS

Loss of B4GALNT1 or ST3GAL5 cause severe changes to neuronal GSL profiles

Cellular disease models were generated using CRISPRi-mediated knock down (KD) of *B4GALNT1* or *ST3GAL5* gene expression. CRISPRi guides targeting these genes were introduced into the dCas9 derivative of the i3N stem cells[27]. For each gene, two knockdown (KD) cell lines using different guide sequences (**Table S1**) were made from the parental dCas9 line: ΔB4GALNT1-1 and -2 to model HSP26; and ΔST3GAL5-1 and -2 to model GM3SD. An additional cell line using a scrambled (SCRM) non-targeting guide in the same dCas9 background was used as a control. Quantitative PCR (qPCR) analysis of neurons confirmed efficient KD of *B4GALNT1* and *ST3GAL5* gene expression (**Fig.1C,D**). mRNA levels were below 2% of SCRM levels in all cell lines except for ΔST3GAL5-2, which retained 9.6% gene expression. Additional qPCR analysis of all cell lines demonstrated expression of neuronal markers (MAP2 and β3-tubulin) confirming that the disease model lines differentiate normally and express relevant markers of neuronal maturity (**Fig.S1**).

Historically, thin-layer chromatography (TLC) has been the primary technique for comparing GSL profiles[31]. However, TLC is limited by the absence of a universal buffer system compatible with all GSL species, meaning unexpected changes in the GSL profile can be missed. Additionally, it is intrinsically qualitative and so doesn't allow accurate quantitation across samples. Quantification of individual GSL species from cells is difficult using mass spectrometry due to several glycan moieties possessing the same molecular mass and the heterogeneity of individual species due to ceramide backbone differences[32]. An alternative strategy to accurately quantify the abundance of different ganglioside headgroups involves enzymatically cleaving and labelling the glycan headgroups specifically from GSLs[33–35]. Briefly, lipids including GSLs are extracted from cell lysates, the ceramide tails of GSLs are cleaved using endocerebrosidase and the glycan headgroups are fluorescently labelled with 2-anthranilic acid. The labelled headgroups are then separated using HPLC for quantification of individual peaks against known standards. To understand how the GSL profile was altered in the HSP26 and GM3SD disease models, this enzymatic approach was employed to quantify the abundance of all ganglioside species (**Fig.1E, S2,S3**). All four KD cell lines show significant loss of the major neuronal gangliosides including

GM1a, GD1b, GD1a and GT1b, as well as the simpler gangliosides GM2 and GD2. Interestingly, the other changes to the GSL profile differed significantly between the two disease models.

Disruption of *B4GALNT1* expression results in an enormous accumulation of the precursor GSLs GM3 and GD3 (**Fig.1E,F**). As these are both direct substrates of B4GALNT1 in the metabolic pathway this is an expected consequence of this genetic disruption. Interestingly, another B4GALNT1 substrate, lactosylceramide (LacCer), also accumulates but to a lesser extent supporting that the presence of ST3GAL5 in this cell line efficiently converts LacCer to GM3. The ΔB4GALNT1 neurons therefore have a very simple GSL repertoire consisting primarily of only two sialylated GSLs, GM3 and GD3. Neither of these GSLs are normally abundant in healthy neurons as they are almost completely converted in the Golgi to more complex GSLs.

Unlike the ΔB4GALNT1 cell line, loss of *ST3GAL5* expression results in accumulation of high levels of the precursor lipid LacCer. Some of this precursor GSL is converted to the o-series GSLs GA2, GA1, GM1b and GD1α. These GSLs are not normally present in neurons, and the presence of B4GALNT1 in these cells has mediated production of this lipid class in the ΔST3GAL5 neurons. Surprisingly, there is also the appearance of globo-series GSLs: Gb3, Gb4 and Gb5 (also known as SSEA3). These GSLs are also not usually present in neurons, normally being enriched on non-neuronal cells including red blood cells and stem cells[36,37]. The enzyme A4GALT is responsible for the conversion of LacCer to Gb3[38]. *A4GALT* gene expression is very low in healthy neurons and in SCRM neurons explaining why no globo-series GSLs are normally present in neurons[27]. *A4GALT* expression was not upregulated in response to ST3GAL5 KD, supporting that the production of globo-GSLs is the result of abnormally increased levels of the LacCer substrate rather than gene dysregulation (**Fig.1G**). These analyses demonstrate that the GSL repertoire of the ΔST3GAL5 neurons has shifted away from the sialylated neuronal GSL species to a complex combination of different non-neuronal, primarily non-sialylated GSLs (**Fig.1F**).

ST3GAL5 disruption severely impacts neuronal firing

To explore the impact of GSL repertoire changes on neuronal function, electrical activity was measured using a multi-electrode array (MEA). MEA allows for the non-destructive monitoring of spontaneous electrical signalling of neurons over time. Neurons were cultured on 24-well MEA plates and electrical signalling was monitored via an array of electrodes with each electrode measuring spikes of field potential. Electrical activity was measured from when neurons start becoming electrically active at around 14 days post-induction (dpi) until 35 dpi. The level of

activity, measured as total number of spikes, increased over time in all cell lines but was severely and consistently reduced in the ΔST3GAL5 neurons (**Fig.2A**). This reduced spike count is clearly evident in the individual timecourse measurements taken at 28 dpi and 35 dpi (**Fig.2B,C** and **S4A,B**). The extent of this disruption in ΔST3GAL5 neurons varied across independently differentiated replicates (**Fig. S5,6**) but across the entire 35-day time period the number of spikes consistently failed to reach SCRM levels. This strong phenotype was not consistently observed in the ΔB4GALNT1 neurons (**Fig.2A** and **S4-6**) suggesting the ΔST3GAL5 neurons have a distinct defect in formation or propagation of electrical signals.

In addition to spike counts, MEA measurements can be analysed in terms of electrical bursts and network bursts (NWB). When >5 spikes were measured on a single electrode within 100 ms these were considered bursts, and when >35% of electrodes in a well registered bursts this was considered a NWB. SCRM neurons displayed strongly synchronized activity across the well from around 24 dpi with a regular pattern of NWB established from 28 dpi (**Fig.2B,** *triangles*, **Fig.S5-7**). Despite evidence for synchronous activity in ΔST3GAL5 neurons at 28 dpi, usually these did not meet the criteria to be a NWB due to the reduced number of spikes (**Fig.2B,** *asterisks*). As the electrical activity of ΔST3GAL5 neurons increased over time, these events crossed the threshold to be considered NWBs (**Fig.2C**) allowing for analysis of NWB behaviour at 35 dpi. Notably, the duration and number of spikes per NWB were significantly reduced in ΔST3GAL5 neurones (**Fig.2D, S4D-F**). However, no difference was seen in NWB frequency across cell lines (**Fig.2E**). ΔB4GALNT1 neurons display no significant reduction in mean duration or spikes per NWB (**Fig.2D, S4C-F**) although there was substantial variability, including several examples of very weak NWB behaviour (**Fig.2B**). The delayed and reduced electrical activity in ΔST3GAL5 neurons suggests the cells have impaired formation or function of synapses that is not seen in ΔB4GALNT1 neurons. In addition to probing the intensity of activity, MEA measurements also allow investigation into coordination of signalling through measurements of synchrony. The area under normalized cross correlation (AUNCC) measures how often and strongly neurons co-activate. The AUNCC is consistently reduced in the ΔST3GAL5 but not ΔB4GALNT1 neurons (**Fig.2F, S4G-H**). Taken together, this suggests the ΔST3GAL5 neurons have disrupted coordination of signalling in addition to reduced activity.

Removal of globo- or o-series GSLs does not rescue the ST3GAL5 disrupted electrical firing

Gangliosides are the only highly abundant GSLs found in healthy neurons, and both ΔST3GAL5 and ΔB4GALNT1 neurons have large reductions in ganglioside abundance. However, only

ΔST3GAL5 neurons have a severe electrical signalling phenotype. Therefore, either ΔB4GALNT1 neurons can better compensate for the loss of gangliosides or ΔST3GAL5 have an additional change in their GSL composition that is responsible for the disrupted electrical signalling. ΔST3GAL5 neurons have increased abundance of the non-neuronal globoside and o-series GSLs. To test whether disruption to electrical signalling in ΔST3GAL5 neurons is due to gain of globoside or o-series GSLs, double KD lines were generated.

To remove the globoside or o-series GSLs, guide RNAs were introduced into the ΔST3GAL5 background targeting the *A4GALT or B4GALNT1* genes respectively (**Fig. 3A**). qPCR of neurons at 28 dpi confirms efficient KD of *ST3GAL5* is maintained in all cell lines as well as efficient KD of additional genes in the respective double knockdowns (**Fig.3B**). GSL profiling confirms that in all KD lines significant reduction of ganglioside abundance is maintained or enhanced (**Fig. 3C**). Although KD of *B4GALNT1* expression in the ΔST3GAL5 background was the least efficient, at <15% of SCRM, it was still sufficient to reduce o-series (GA2, GA1, GM1b) GSLs abundance back to near-normal levels (**Fig. 3C, S8**). Notably, in this double KD a single GSL, LacCer, now represents almost 80% of the total GSLs in these neurons. Although expression of A4GALT is already very low in neurons, KD of this gene in the ΔST3GAL5 background, to <5% of SCRM, reduces the globoside GSLs Gb3 and Gb4 back to normal levels (**Fig. 3C, S8**).

MEA analysis of electrical firing of these different compound KD lines demonstrates that loss of *A4GALT* or *B4GALNT1* expression and consequent removal of globoside or o-series GSLs, respectively, does not rescue the electrical signalling phenotype observed in ΔST3GAL5 neurons (**Fig.S9-11**). Number of spikes (**Fig.3D, S11D-E**), area under normalized cross correlation (**Fig.3E, S11F-G**), spikes per NWB and NWB duration (**Fig.S11A-B** and **H-K**) remain significantly reduced in all double KD lines compared to SCRM. This supports that the accumulation of globoside or o-series lipids are not the cause of the reduced electrical activity or disrupted coordination of signalling observed in ΔST3GAL5 neurons. Instead, it suggests that the precursors that accumulate in ΔB4GALNT1 neurons are better able to compensate for the loss of gangliosides than the globoside and o-series GSLs that accumulate in ΔST3GAL5 neurons. As LacCer accumulates in all KD lines including ΔB4GALNT1, it seems likely that GM3 and GD3 are the precursor GSLs responsible for this compensation (**Fig.1E** and **3C**). A notable common feature of GM3, GD3 and all the gangliosides that is not shared with the globoside or all o-series GSLs, is they contain a sialic acid moeity. Despite the relatively simple structure of these precursors, the GSL composition in ΔB4GALNT1 neurons retains a high abundance (>80%) of sialylated GSLs, similar to that of healthy neurons and distinct from that of the other KD models (**Fig. 3F**). Therefore, it is likely that this sialic acid moiety is important for why GD3 and GM3 can partially

compensate for the loss of complex gangliosides, whereas the globoside and o-series lipids cannot. In further support of this hypothesis, the ΔST3GAL5+ΔB4GALNT1 neurons that possess the lowest abundance of sialylated GSLs also demonstrate the strongest electrical deficiencies (**Fig.3D-F, S11**).

Loss of sialylated GSLs has a significant impact on the protein repertoire of the plasma membrane

Previous work has demonstrated that disruption of GSL metabolism can alter the protein composition of the PM[4,28,39]. Alterations to the PM proteome might thus explain the disruption to electrical firing in ΔST3GAL5 neurons. Importantly, comparison of the PM proteomes of the ΔST3GAL5 and ΔB4GALNT1 disease models allow for the dissection of which GSLs are most critical for protein delivery and stability at the PM, as well as which proteins could be contributing to the disrupted electrical phenotype. As SCRM neurons have formed mature functional synapses by 28 dpi but ΔST3GAL5 neurons have not established sustained NWBs (**Fig.2B**), this time point represents a particularly interesting stage in the development of network behaviour and was chosen for molecular analyses. Due to the relatively low abundance of individual membrane proteins, the PM composition was profiled using aminooxy-biotin labelling of intact cells and enrichment of proteins with streptavidin prior to mass spectrometry analysis. Proteomics datasets were filtered to remove non-PM proteins and data from the two individual guides for each KD were combined. High-confidence targets were selected based on a significant change (<0.05 adjusted *p*-value) in abundance of at least 1.65-fold compared to SCRM controls. Abundance changes are displayed as volcano plots and reveal substantial loss of several PM proteins in ΔST3GAL5 (**Fig.4A** and **Tables S2-3**) yet almost no changes in the ΔB4GALNT1 neurons (**Fig.4B** and **Tables S4-5**).

Interestingly, there was a decrease in the total abundance of peptide and number of quantified PM proteins in the ΔST3GAL5 samples compared to the SCRM despite normalisation of the whole sample protein concentration prior to PM protein enrichment (**Fig.4C,D**). The drop in quantified proteins and peptide is not observed in ΔB4GALNT1 neurons (**Fig.4E,F**) suggesting that the loss of sialylated GSLs has significantly altered the capacity of ΔST3GAL5 neurons to deliver and/or retain membrane proteins at the PM. A significant drop in peptide or protein abundance is not seen in the whole-cell proteome of ΔST3GAL5 or ΔB4GALNT1 neurons and very few proteins are significantly changed in abundance in either cell line compared to SCRM (**Fig.4G,H** and **Tables S6-8**). This suggests that observed changes in protein abundance at the PM are caused by

mislocalisation of proteins rather than overall changes in protein expression, synthesis or stability.

Due to the large-scale remodelling of the plasma membrane proteome it is highly likely that no single change is the key determinant of disrupted electrical signalling or ST3GAL5-associated disease, and that this is instead a complex consequence of the large number of proteins lost from the PM. Proteins that may be directly contributing to disrupted electrical activity include voltage- and ligand-gated ion channels, which are essential for synaptic function and electrical signalling. Five ion channels are significantly downregulated from the PM in ΔST3GAL5 neurons (HCN2, KCNH7, KCNA3, CLCN4 and HTR3A). The voltage-gated, non-selective cation channel HCN2 is important for controlling conduction velocity, setting the resting membrane potential and ensuring rhythmic firing of neurons[40–42]. Voltage-gated Na^+ channels enable rapid depolarization during action potential and voltage-gated K^+ channels such as KCNH7 (a.k.a. ERG3) and KCNA3 (a.k.a. Kv1.3) are required to stabilize the resting potential and repolarize the membrane[43,44]. Ligand-gated channels such as the serotonin-activated HTR3A mediate rapid synaptic transmission in response to neurotransmitters[45]. CLCN4 (a.k.a. ClC-4) is a predominantly intracellular Cl^- channel but has been identified at the PM of neurons[46]. All five of these channels have been associated with epilepsy and other neurological diseases[44,47–51].

Another group of proteins that could contribute to ST3GAL5-associated disease are G-protein coupled receptors (GPCRs), which are a diverse class of membrane receptors that are localised to GSL-rich membrane microdomains and are activated by extracellular stimuli such as neurotransmitters. Seven GPCRs (CHRM4, CXCR4, KISS1R, NPY1R, OPRL1, PTGER3, TRHR) are significantly downregulated from the PM in ΔST3GAL5 neurons. Activation of GPCRs can influence effector proteins and the production of second messengers such as cAMP which is crucial for the function of pre- and post-synaptic plasticity. GPCRs play key roles in regulating ion channel activity and neurotransmitter release and so a loss in their abundance at the cell surface is likely to disrupt electrical signalling. Although the activity of some of these GPCRs may not be triggered in a monoculture of cortical glutamatergic neurons, the reduced abundance of these at the PM remains relevant for ST3GAL5-associated disease.

Transmission of electrical and chemical signals across synapses, mediated in part by ion channels and GPCRs requires coordinated formation and organization of synapses. Pre- and post- synaptic adhesion molecules such as NRXN3 and LRRTM3, both of which are

downregulated in ΔST3GAL5 neurons play major roles in modulating this organization as well as influencing synaptic plasticity[52–55].

A small number of proteins appear upregulated at the surface of ΔST3GAL5 neurons (**Fig. 4A**). However, most of these were quantified in SCRM neurons but not in ΔST3GAL5 neurons and the appearance of them being upregulated is likely an artefact of imputation (**Fig. S12**).

DISCUSSION

The detailed comparison of human iPSC-derived neuronal models of ST3GAL5 and B4GALNT1 deficiency has shed new light on the relationship between GSL composition and cellular function. By expanding these models into dual knockdowns, we clearly demonstrate that it is the loss of sialylated neuronal gangliosides, rather than the gain of non-neuronal GSLs, that disrupts propagation and coordination of electrical signalling. Furthermore, we demonstrate that the synthesis of simple, unbranched sialylated GSLs can prevent this signalling defect, highlighting the essential role of lipid sialylation for neuronal function. Mechanistic insights into disease pathology are demonstrated by the contrasting PM proteome profiles of these two models of distinct GSL metabolic defects. The absence of sialylated GSLs in the ΔST3GAL5 neurons causes substantial loss of PM proteins, several of which are crucial for neuronal functions. This loss explains the electrophysiological phenotype in ΔST3GAL5 neurons and allows for a mechanistic understanding of the severe neurological phenotypes in GM3SD patients. Importantly, the presence of simple sialylated GSLs in ΔB4GALNT1 neurons can, to some extent, compensate for this loss as demonstrated by almost wildtype electrical firing and an essentially unchanged PM proteome.

While ΔST3GAL5 mouse models of GM3SD display metabolic and behavioural changes, they lack the microcephaly, severe neurodevelopmental delay and epilepsy that is characteristic of the human condition[18,56,57]. It is unlikely this reflects a different dependence on gangliosides as ΔST3GAL5+ΔB4GALNT1 mice develop severe neurodegenerative processes after weaning and die at 2-3 months old, supporting that gangliosides are essential for the higher order development of the mouse CNS[58,59]. Instead, it suggests loss of function mutations in ST3GAL5 differentially affect the GSL profile of mice and humans, resulting in different severities of disease. Samples from the brains of ΔST3GAL5 mice[18,57,60], plasma and fibroblasts of GM3SD patients[6,8,9,11,61], and the ΔST3GAL5 neurons presented here all show decreased abundance of gangliosides and sialylated precursors (GD3 and GM3). In patient samples there is an accumulation of globosides[6,9,61] which is also seen in our iPSC models, alongside an

accumulation of non-sialylated o-series lipids (GA2, GA1). None of these GSLs accumulate in mice. To examine whether these alternative GSLs were conferring the electrophysiological phenotypes we made compound KD lines to remove these non-neuronal lipids, but the data demonstrate they were not driving the disease phenotypes. The important difference is that the human ΔST3GAL5 GSL profile is dominated by non-sialylated lipids, whereas the dominant species in the brains of ΔST3GAL5 mice are the sialylated o-series lipids GM1b and GD1α[6,8,9,11,18,57,60,61]. GD1α could be particularly significant because it is mostly absent in human samples and, although it lacks a sialic acid on the first galactose (as found in GM3, GD3 and gangliosides), it carries a sialic acid on the subsequent glycan. This, in combination with a greater proportion of GM1b could be sufficient to partially compensate and reduce the severity of disease in mice. An alternative explanation is that there are additional compensating GSL species in the mouse brain that have not yet been detected, potentially due to limitations of thin-layer chromatography. Using the glycan cleavage method employed here may give a more complete and quantitative profile.

Unlike ST3GAL5, loss of function mutations in B4GALNT1 have comparable consequences in mice and humans, such as presenting with gait and motor defects with underlying peripheral axonal degeneration[7,16,21,22,62]. This likely reflects their shared changes to the GSL profile with decreased abundance of gangliosides and increased GM3 and GD3 observed in both mice[62–66] and in our ΔB4GALNT1 neurons. The proteome (**Fig.4**) and electrical firing (**Fig.2&3**) of ΔB4GALNT1 cells show little change, even though both patients and mice present with neurodegenerative disease. This finding suggests that the presence of GM3 and GD3 may offer only short-term or partial compensation for the loss of gangliosides. This is supported by a delayed onset of disease, with HSP26 patients typically experiencing symptoms aged 3-19 years old, whereas GM3SD sufferers present in the first 3 months of life with epilepsy often developing in the first year[7,9,67]. It is possible that while the short sialyated GSLs (GM3 and GD3) are able to traffic proteins to the cell surface they are not able to maintain their long-term localization or stably maintain microdomain formation. GD3 appears particularly important for this compensation because over two thirds of mice that have only GM3 die before reaching 30 weeks of age[68,69].

The question remains as to why the loss of the sialylated GSLs has such a profound impact on the PM proteome. Are these proteins not delivered to the PM or are they being prematurely internalized? Extensive evidence supports the role of GSLs in biosynthetic sorting in the late secretory pathway, including recycling of membrane proteins to and from the PM, but specific details for how different GSLs contribute to sorting remains elusive[70–75]. There is also growing

evidence supporting the importance of glycans, particularly sialylated ones, on both proteins and lipids for modulating endocytosis, with glycan-binding galectins playing crucial roles in tuning endocytic processes[76]. Glycolipid-lectin-driven endocytosis is a clathrin-independent mechanism for membrane protein internalization, with the clustering of GSL-bound oligomeric lectins inducing membrane bending to form endocytic pits[76–79]. Although there is evidence that this process is cargo-specific, the exact glycan structures to which galectins bind on GSLs, the relevant cargoes, and the mechanism by which oligomerization affects this process remain to be determined[76,80]. Previous work exploring how viruses and toxins use GSLs for cell entry proposes that the position of the sialic acid on a GSL contributes to the delivery of extracellular cargoes to different intracellular compartments[81]. However, the details of these mechanisms remain extremely challenging to dissect due to the promiscuous GSL binding of pathogen-related proteins[82–85].

Our observations here and previously have identified that different subsets of proteins are changed in their PM abundance depending on how the GSL repertoire of a cell has been altered[28,39]. This supports some level of specificity in the disruption rather than a general impact on membrane microdomain structures or membrane dynamics. This specificity could be driven by direct interactions between the extracellular domains (ECDs) of these proteins and the GSL headgroups. There is substantial evidence that such interactions occur, but it is again extremely challenging to dissect the specificity of these interactions or to identify which interaction is the most critical for PM protein delivery and stability[86–88]. Indeed, several GSL-binding proteins interact with distinct GSL headgroups and this can modulate their activity[89–91]. However, as the large, branched GSL headgroups contain within their structure the smaller, simpler headgroup moieties there is an intrinsic capacity for a GSL-binding protein to also interact with smaller headgroups, albeit more weakly. This is potentially consistent with our observed capacity for GM3/GD3 to restore membrane trafficking, but to still leave cells prone to longer-term degeneration.

Our data support that GM3SD is not only a lipid metabolic disorder but can also be considered a secondary channelopathy/synaptopathy driven by lipid-dependent protein mislocalisation. A challenge in interpreting functional readouts of our GM3SD model is the lack of comparative MEA datasets across 'pure' developmental disorders versus 'pure' primary epilepsies. Without these benchmarks, it is difficult to deconvolute whether the failure of ΔST3GAL5 neurons to establish sustained network bursts is a definitive indicator of a developmental delay, a signature of circuit instability leading to epilepsy, or a combination of both. Although the phenotypic observations recorded in ΔST3GAL5 neurons are likely a combinatory effect of multiple proteins being lost from

the PM, examining the established contributions of these proteins to neurological disorders offers functional insights into the drivers of pathogenesis. Three groups of proteins identified in the PMP stand out as potential drivers of observed phenotypes: ion channels, GPCRs and adhesion molecules. Amongst the five significantly downregulated ion channels, HTR3A[92] and HCN2[93] are responsible for depolarisation of neurons. HCN2, in particular, is involved in both neurodevelopmental disorders[48] and epileptogenesis[49,94]. However, the impact of HCN channels on neuronal excitability is inherently complex because they exhibit a "dual nature": while their opening depolarizes the membrane and increases excitability, it also decreases membrane resistance, which dampens excitability[40]. In contrast to the depolarising hits, the voltage-gated potassium channels KCNA3 and KCNH7 are essential for repolarisation[43,44]. KCNA3 is linked to both developmental and epileptic disorders[44,50], and KCNH7 has implications in epilepsy[51]. This suggests that both depolarisation and repolarisation processes may be profoundly affected in ΔST3GAL5 neurons.

In addition to ion channels that can directly cause neuronal firing defects, changes in GPCRs and adhesion molecules represent a more nuanced layer of disruption. One particularly relevant example of this modulatory crosstalk is the downregulation of KISS1R and NPY1R, the two most significantly depleted GPCRs in our dataset. Both receptors affect the accumulation of intracellular cAMP[95,96], a second messenger that regulates the activity of HCN channels[97]. In addition, the therapeutic potential demonstrated by the respective ligands of these receptors, kisspeptin[98] and neuropeptide Y[99], in epilepsy further underscores the relevance of these GPCRs in general seizures. However, it is worth noting that several drugs that are used for treating epilepsies do not provide long-term relief in GM3SD, suggesting that the therapeutic targets of these small molecules may themselves be downregulated from the PM[100].

Intriguingly, a subset of the downregulated proteins in our PMP dataset, such as LRRTM3[101], CXCR4[102] and HCN2[103], are associated with late-onset neurodegenerative pathologies such as Alzheimer's disease. Furthermore, in neuronal models of early-onset neurodegenerative lysosomal storage disorders (LSDs), caused by accumulation of gangliosides, we also see PM protein remodelling including the loss of CXCR4 and NRXN3[28]. Given the involvement of membrane microdomains in Alzheimer's[104], Parkinson's disease[105] and LSDs[106–108], PM protein depletion driven by GSL alterations may be a shared mechanistic link disrupting microdomain-dependent proteostasis.

The alterations to the PM proteome observed in ΔST3GAL5 neurons reveals a pathological landscape of immense complexity. As several of the PM proteins identified here are functionally

interdependent, the resulting phenotype represents a complex 'system failure'. Consequently, it is highly unlikely that any single pharmacological intervention could simultaneously rescue the multiple different molecular changes. The only feasible therapeutic strategy is likely to be a gene therapy-based replacement of ST3GAL5 expression to reconstitute the sialylated ganglioside repertoire required to restore PM functional integrity.

MATERIALS AND METHODS

Cell line maintenance

Human CRISPRi-i3N stem cells[26] carrying a stably integrated dCas9 construct were cultured at 37 °C and 5% CO_2 in complete E8 medium (Gibco™), with daily medium changes. Cells were grown on Matrigel-coated plates (1:50 dilution in DMEM/F-12 HEPES; Gibco™). For passaging, cells were detached either with 0.5 mM EDTA and re-plated as colonies in E8 medium, or with Accutase and re-plated as single cells in E8 medium supplemented with 50 nM chroman-1 (Tocris).

Differentiation of stem cells into neurons was performed as previously described, with minor modifications[26]. Following Accutase dissociation, 7×10^6 or 1.5×10^7 stem cells were seeded onto 10 or 15-cm Matrigel-coated dishes respectively. Cells were seeded in induction medium (IM), consisting of DMEM/F-12 HEPES supplemented with 1× N2, 1× NEAA, 1× GlutaMAX, and 2 µg/ml doxycycline. During initial plating, IM was additionally supplemented with 10 µM chroman-1, and the medium was replaced daily for the first three days.

Partially differentiated neurons were dissociated with Accutase and re-plated onto dishes coated with 100 µg/ml poly-L-ornithine (PLO) in cortical neuron (CN) medium, consisting of Neurobasal Plus supplemented with 1× B27, 10 ng/ml NT-3 (PeproTech), 10 ng/ml BDNF (PeproTech), and 1 µg/ml laminin. During re-plating, CN medium was supplemented with 1 µg/ml doxycycline. From this point onward, half-medium changes were performed three times per week.

Generation of CRISPR knockdown cell lines

Guide RNAs targeting ST3GAL5, B4GALNT1 and A4GALT were designed using Dharmacon or the CRISPick server (Broad Institute; **Table S1**), selecting sites at or immediately upstream of the first exon. For targeting of a single gene, complementary oligonucleotides with appropriate overhangs were annealed and cloned into the BpiI site of the pKLV backbone (gift from the Prof. Evan Reid, Cambridge). For targeting a second gene, oligonucleotides were cloned into the BsmB1 site of

the lentiCRISPRv2 backbone with a hygromycin resistance cassette (gift from Prof. Evan Reid, Cambridge)[109].

For lentiviral production, HEK293T cells were cultured in DMEM supplemented with 10% FBS at 37 °C and 5% CO_2 and passaged twice weekly using Trypsin-EDTA. A total of 2×10^6 cells were transfected in OptiMEM with 8 µl TransIT and 2 µg of plasmid DNA at a 3:2:1 ratio of CRISPRi pKLV construct:pCMVΔ8.91:pMD.G. The transfection mixture was added dropwise, and after 24 h the medium was replaced with E8. At 48 h post-transfection, the virus-containing E8 medium was collected, 0.45µm filtered to remove debris and stored at -70 °C.

5×10^5 i3N stem cells were transduced with 2 ml of a 1:1 mixture of complete E8 medium and lentiviral supernatant supplemented with 50 nM chroman-1 and 10 µg/ml polybrene. Cells were seeded on Matrigel-coated 6-well plates and then transferred to 37 °C for incubation. After 24 h, the medium was replaced with fresh E8. At 48 h post-transduction, cells were switched to E8 medium containing 1 µg/ml puromycin, which was refreshed daily for at least 7 days. Surviving cells were subsequently maintained in puromycin-free E8 medium.

Quantitative PCR (qPCR)

RNA was extracted from 2×10^6 cells using the PureLink RNA extraction kit (Invitrogen) following the manufacturer's protocol. cDNA was generated from purified RNA using the High-Capacity RNA-to-cDNA kit (Applied Biosystems) following the manufacturer's protocol. qPCR reactions contained 1× TaqMan Fast Advanced Master Mix (Applied Biosystems), 50 ng cDNA, and 1× FAM-labelled TaqMan Gene Expression Assays (Applied Biosystems) specific to each target gene (**Table S9**). Reactions were run on a CFX96 Real-Time System (Bio-Rad), starting with 10 mins at 95 °C, followed by 40 cycles of 95 °C for 15 s and 60 °C for 1 min. Each experiment included n = 3 technical replicates per gene and N = 3 independent biological replicates. Gene expression changes were quantified using the ΔΔCt method with GAPDH as the reference gene[110]. Statistical significance of fold changes was assessed by two-way ANOVA with Dunnett's multiple comparisons testing

Quantification of gangliosides by HPLC

Glycosphingolipids were analysed as previously described[34,35]. Briefly, lipids were extracted from 2×10^6 cells using a 4:8:3 chloroform:methanol:water mixture and purified via C18 solid-phase extraction (Telos, Kinesis). Bound lipid species were eluted twice with 1 mL 98:2 chloroform:methanol, followed by two 1 mL elutions of 1:3 chloroform:methanol and a final 1 mL methanol wash. Eluates were dried under a stream of nitrogen gas and digested overnight with

recombinant endoglycoceramidase I (gift from the Platt Lab, Oxford). Released glycans were labelled with 2-anthranilic acid (2AA) and purified using DPA-6S amide SPE columns (Supelco). Purified 2AA-labelled glycans were separated and quantified by normal-phase HPLC. Peak areas were compared with a 2.5 pmol 2AA-labelled chitotriose standard (Ludger) to calculate absolute values, and values were presented as percentage GSL abundance for ease of comparison between samples. Glycan species were identified by matching retention times to a reference standard of commercially available gangliosides. Chromatographic separation was performed on a TSKgel Amide-80 column (Anachem) using a Waters Alliance 2695 separations module with an in-line Waters 2475 multi λ-fluorescence detector (excitation 360 nm, emission 425 nm). All runs were conducted at 30 °C using solvent compositions and gradient conditions described previously[34,35]. Experiments were performed in biological triplicate, and differences in ganglioside abundance were assessed by two-way ANOVA with Dunnett's multiple comparisons testing.

Proteomics

Proteomics cell culture. Cell lines were differentiated in triplicate to generate three independent biological replicates. Partially differentiated 3 dpi i3N cultures of SCRM, ΔST3GAL5-1 and ΔST3GAL5-2 or SCRM, ΔB4GALNT1-1, and ΔB4GALNT1-2 were seeded onto PLO-coated plates. For whole-cell proteomics (WCP) cells were seeded at 2×10^6 cells per well of a 6-well plate and for plasma membrane proteomics (PMP) at 1×10^7 cells per 10-cm dish. Cultures were maintained until 28 dpi with half-medium changes performed thrice weekly. Cells were washed three times with PBS and scraped into low-bind Eppendorf tubes. Pellets were collected at 500 × g for 10 min, PBS was removed, and samples were snap-frozen in liquid nitrogen and stored at -70 °C until simultaneous processing of biological replicates. WCP samples were analysed using tandem mass tag (TMT) labelling and data-dependent acquisition (DDA). PMP samples were analysed using label-free data-independent acquisition (DIA) mass spectrometry.

Sample preparation for WCP. Cell pellets were resuspended and lysed in 6 M guanidine hydrochloride/50 mM HEPES, pH 8.5. Samples were vortexed extensively, sonicated in a cold water-bath sonicator using five 30 s pulses, and clarified by centrifugation at 13,000 × g for 10 min at 4 °C. The supernatant was transferred to a fresh tube and centrifuged again under the same conditions. Proteins were reduced with DTT (final concentration 5 mM) for 20-30 min shaking at 56 °C, alkylated with iodoacetamide (final concentration 14 mM) for 20-30 min shaking at room temperature in the dark, and excess iodoacetamide was quenched by addition of further DTT (final concentration 9 mM) followed by incubation for 15 min at room temperature. Samples were

then diluted with 200 mM HEPES, pH 8.5 to reduce the guanidine concentration to 1.5 M and digested with LysC for 3 h at room temperature. Samples were subsequently diluted further to 0.5 M guanidine with 200 mM HEPES, pH 8.5, supplemented with trypsin to a final concentration of 3.33 ng/µL, and incubated shaking overnight at 37 °C. The following day, digests were acidified with formic acid (final concentration 2.5% v/v) and centrifuged at 21,000 × g for 10 min, and the clarified supernatant was transferred to a fresh tube for peptide clean-up. Peptides were purified using 50 mg C18 Sep-Pak cartridges that were activated with acetonitrile and then formic acid-containing buffer (70% acetonitrile, 1% formic acid) before equilibration into 1% formic acid. After sample loading, cartridges were washed with 1% formic acid and peptides were eluted with formic acid-containing buffer (70% acetonitrile, 1% formic acid)

Eluates were dried by vacuum centrifugation and resuspended in 200 mM HEPES or 150 mM TEAB, pH 8.5. Peptide concentration was determined by micro-BCA assay, and 25-40 µg of peptide were taken forward for TMT labelling. For labelling, samples were adjusted to 40 µL in 200 mM HEPES, pH 8.5 and to a final acetonitrile concentration of 30%, then reacted with 5 µL TMT reagent (18.6 µg/ µL in anhydrous acetonitrile) for 1 h at room temperature. Reactions were quenched by addition of 5% hydroxylamine to a final concentration of approximately 0.5% and incubated for 15 min, after which samples were acidified to approximately 1% formic acid. Labelled samples were then combined in equal peptide amounts, and residual free tag was removed by a further Sep-Pak clean-up. Briefly, the Sep-Pak cartridge was wetted with 1 mL of 100% methanol, then by 1 mL acetonitrile, equilibrated with 1 mL of 0.1% trifluoracetic acid and the sample was loaded slowly. The cartridge was washed 3x with 1 mL trifluoracetic acid before eluting sequentially with 250 µL of 40% acetonitrile, 70% acetonitrile and 80% acetonitrile, before being dried in a vacuum centrifuge.

The peptides were fractionated by high-pH reverse-phase chromatography using an Ultimate 3000 ultra-high-performance chromatography (UHPLC) system (Thermo Scientific) equipped with a Kinetex Evo C18 (1.7 µm, 2.1 × 150 mm) column (Phenomenex). The mobile phase used were, HPLC-grade water 3:97(v/v) (eluent A); 100% LCMS-grade acetonitrile (eluent B) and 200 mM ammonium formate in HPLC-grade water, pH 10 (eluent C). Eluent C was maintained at 10%, while A and B were altered over the fractionation gradient. The elution gradient was 0-19% B in 10 min; 19-34% B in 14.25 min and 34-50% B in 8.75 min, followed by a 10 min wash of 90% B. Flow was set at 0.20 mL/min for the first 5 min while peptides which were reconstituted in 40 µL of eluent C were loaded onto the column. Thereafter the flowrate was increased to 0.40 mL/min for the rest of the protocol. 168 fractions were collected every 0.25 min between 10 and 52 min of

the fractionation run. The fractions were concatenated into 12 pools and reduced to dryness in a refrigerated vacuum centrifuge.

Sample preparation for PMP. Sialic acids on the extracellular surface of plasma-membrane proteins were oxidized with sodium periodate to generate aldehydes, followed by aniline-catalysed oxime ligation with aminooxy-biotin. For biotinylation, 10 cm dishes of cells were washed three times with 5 ml ice-cold PBS (pH 7.4) and incubated in 5 ml biotinylation solution (1 mM sodium periodate, 100 µM aminooxy-biotin, 10 mM aniline in ice-cold PBS pH 6.7). Plates were wrapped in foil and rocked at 4 °C for 30 min. Reactions were quenched with 5 ml 2 mM glycerol, removed, and cells were washed three times with ice-cold PBS pH 7.4. PBS was aspirated completely and cells were scraped into 500 µl lysis buffer (10 mM Tris pH 7.4, 1% Triton X-100, 150 mM NaCl, 5 mM EDTA, protease inhibitors) in low-bind tubes. Lysis was performed by end-over-end rotation for 1.5 h at 4 °C. Lysates were cleared by centrifugation at 20,000 × g for 10 min, and supernatants were transferred to fresh low-bind tubes, snap-frozen in liquid nitrogen, and stored at -70 °C until enrichment. Frozen lysates were thawed and quantified by BCA assay. Protein concentrations were equalized using lysis buffer so that all samples contributed identical total protein mass to enrichment. High Capacity NeutrAvidin Agarose Resin (Thermo Scientific, 50 µL slurry per sample) were washed four times with 1 ml lysis buffer (resuspension, 500 × g for 5 min, aspiration, repeat). Normalized lysates were added to the washed beads and incubated by end-over-end rotation for 2.5 h at 4 °C. For washing, bead-lysate mixtures were transferred onto SnapCap filter columns (Pierce) mounted on a vacuum manifold. After draining, beads were washed sequentially with 20 × 400 µL lysis buffer, 20 × 400 µL 0.5% SDS in PBS pH 7.4, and 10 × 400 µL urea buffer (6 M urea, 50 mM TEAB, pH 8.5). Columns were removed, capped, and beads were incubated with 400 µL reduction/alkylation solution (10 mM TCEP, 20 mM iodoacetamide in urea buffer) for 30 min at room temperature in the dark with shaking at 850 rpm. Columns were returned to the manifold, drained, and washed an additional 10x with urea buffer. Beads were then resuspended in 400 µL 50 mM TEAB and transferred to low-adhesion tubes. Columns were rinsed twice more with 400 µL TEAB and the rinses were pooled with the bead suspension. Beads were pelleted at 500 × g for 2 min and supernatant was removed. Beads were resuspended in 50 µL of 50 mM TEAB containing 0.5 µg MS-grade trypsin (Pierce; stock 1 µg/µL in 50 mM acetic acid) and digested overnight at 37 °C with shaking at 850 rpm. The next day, beads were pelleted at 500 × g for 5 min, and the supernatant was collected. Beads were washed with an additional 40 µL of 50 mM TEAB; the wash was pooled with the digest supernatant. Eluates were dried using a vacuum centrifuge and stored at -20 °C.

Mass Spectrometry for WCP samples. Mass spectrometry data for WCP were also acquired by Dr. Robin Antrobus of the CIMR proteomics facility on an Orbitrap Lumos instrument as previously described[111]. Peptides were separated on an RSLC3000 nano-UPLC system equipped with a 300 µm × 5 mm Acclaim PepMap µ-precolumn and a 75 µm × 50 cm, 2.1-µm particle Acclaim PepMap RSLC analytical column. The loading solvent was 0.1% formic acid (FA), and the analytical solvents were 0.1% FA (solvent A) and 80% acetonitrile with 0.1% FA (solvent B). All separations were performed at 40 °C, with samples loaded at 5 µl/min for 5 min before application of one of two gradients: 3-7% B over 4 min and 7-37% B over 173 min followed by a 4-min wash at 95% B and 15-min re-equilibration at 3% B, or 3-7% B over 3 min and 7-37% B over 116 min followed by identical wash and re-equilibration. Quantification used a MultiNotch MS3-based TMT workflow[112], with MS1 acquired from m/z 380-1,500 at 120,000 resolution (2×10^5 AGC target, 50-ms maximum injection time), MS2 acquired in the ion trap following quadrupole isolation (m/z 0.7), CID fragmentation (NCE 34), turbo-scan mode (1.5×10^4 AGC target, 120-ms maximum injection time), and MS3 performed in synchronous precursor selection mode selecting the top 10 MS2 ions for HCD fragmentation (NCE 45) and Orbitrap detection at 60,000 resolution (1×10^5 AGC target, 150-ms maximum injection time). Parallelisable time was disabled, and the full MS1/MS2/MS3 cycle time was 3 s. Mass spectrometry data have been deposited with the ProteomeXchange Consortium via the PRIDE repository.

Mass spectrometry for PMP samples. Mass spectrometry data for PMP were acquired by Dr. Robin Antrobus of the CIMR proteomics facility on a Thermo Q Exactive Plus mass spectrometer (Thermo Scientific) equipped with an EASYspray source and coupled to an RSLC3000 nano-UPLC system. Digested peptides were separated on a 50 cm C18 PepMap EASYspray column maintained at 40 °C at a flow rate of 300 nL/min. A gradient was run using solvent A (0.1% formic acid) and solvent B (80% acetonitrile, 0.1% formic acid), increasing from 3% to 40% solvent B over 90 min, followed by a 5 min wash at 95% solvent B. Full MS spectra were acquired at a resolution of 35,000 across an m/z range of 350-1430, and MS/MS spectra were collected in DIA mode. Fragmentation spectra were acquired at 17,500 FWHM following HCD, using a 30 m/z isolation window, an AGC target of 1×10^6, and a loop count of 18.

Analysis of mass spectrometry data. WCP data was processed in Proteome Discoverer 2.2 using the Sequest search engine and PMP data was processed with default parameters in DIA-NN version 2.2.0[113]. Spectra were searched against the human proteome, downloaded on 11.01.2021 for WCP and 21.05.2025 for PMP. Resulting peptide and protein tables were imported into Perseus[114] for downstream analysis. In Perseus, measured ion abundances were $\log_2$-transformed and data was filtered to remove common contaminants. PMP data was further

filtered to only include proteins annotated with gene ontology cellular compartment (GOCC) terms plasma membrane (GO:0005886), cell surface (GO:0009986), or extracellular region (GO:0005576). WCP and PMP was further filtered to remove proteins not quantified in all three replicates of any one condition and missing values were imputed by fitting to a normal distribution. Replicates a were grouped, and significantly altered proteins were identified using two-sample t-tests with an FDR threshold of <0.05. Fold-change and P-values were used to assign significance and to generate volcano plots, which were visualized in GraphPad Prism 9.

Multi-electrode array (MEA)

Wells of a 24-well MEA CytoView plate (Axion BioSystems, M384-tMEA-24W) were coated with 500 µl 1× PLO and incubated overnight at room temperature. Wells were washed three times with sterile water and allowed to dry for ~1 h before seeding 4×10^5 3 dpi neurons per well in 1 ml CN maintenance medium containing 1 µg/mL doxycycline. Cultures were maintained as described above with thrice weekly half-media changes. Recordings were performed on a Maestro Edge system (Axion BioSystems, 200-0888) using AxiS Navigator software. Activity and viability were routinely monitored with spikes detected using a threshold of 6× the standard deviation. On recording days, plates were equilibrated for >15 min at 37 °C and 5% CO_2 before data acquisition. Spontaneous activity was recorded for 6 min in AxIS. Data were processed using NeuralMetric and the AxIS Plotting Tool before subsequent analysis in GraphPad Prism 9. Electrode bursts were identified using the ISI threshold algorithm in NeuralMetric with default parameters, minimum number of spikes = 5, max inter-spike interval = 100 ms. Network bursts were identified using the ISI threshold algorithm in NeuralMetric with default parameters, minimum number of spikes = 50, max inter-spike interval = 100 ms, minimum electrodes = 35%. Area under normalized cross-correlation (AUNCC) calculated using the cross-correlogram algorithm in NeuralMetric with default parameters, synchrony window = 20 ms.

ACKNOWLEDGEMENTS

This research was funded by a Wellcome Trust grant (219447/Z/19/Z) awarded to JED that paid the salaries of JED, ASN and HGB (https://wellcome.org). ZZH is supported by the Cambridge Trust International Scholarship with additional research funds provided by Altos Labs Inc. FMP is a Wellcome Trust Investigator (202834/Z/16/Z). The salary of FMP was partially supported by a Royal Society Wolfson merit award (WM130016, https://royalsociety.org). The salary of DtV was

partially supported by a Medical and Life Sciences Translational Fund (University of Oxford). The salary of DAP was partially supported by a Mizutani Foundation for Glycoscience grant (200133, https://mizutanifdn.or.jp). The funders had no role in study design, data collection and analysis, decision to publish, or preparation of the manuscript. For the purpose of open access, the author has applied a Creative Commons Attribution (CC BY) license to any Author Accepted Manuscript version arising from this submission.

DATA AVAILABILITY

The mass spectrometry proteomics data have been deposited to the ProteomeXchange Consortium via the PRIDE partner repository with the dataset identifier XXX (https://www.ebi.ac.uk/pride/archive/projects/XXX).

Competing interests: The authors have declared that no competing interests exist in relation to the data in this study.

REFERENCES

1. Hannun YA, Merrill AH, Luberto C. The bioactive sphingolipid playbook. A primer for the uninitiated as well as sphingolipidologists. J Lipid Res. 2025;66: 100813. doi:10.1016/j.jlr.2025.100813

2. Hannun YA, Obeid LM. Sphingolipids and their metabolism in physiology and disease. Nat Rev Mol Cell Biol. 2018;19: 175–191. doi:10.1038/nrm.2017.107

3. Kuo A, Hla T. Regulation of cellular and systemic sphingolipid homeostasis. Nat Rev Mol Cell Biol. 2024; 1–20. doi:10.1038/s41580-024-00742-y

4. Monkhouse H, Deane JE. Linking glycosphingolipid metabolism to disease-related changes in the plasma membrane proteome. Biochem Soc Trans. 2024;52: 2477–2486. doi:10.1042/BST20240315

5. Sandhoff K, Klein A. Intracellular trafficking of glycosphingolipids: role of sphingolipid activator proteins in the topology of endocytosis and lysosomal digestion. FEBS Lett. 1994;346: 103–107. doi:10.1016/0014-5793(94)00282-7

6. Simpson MA, Cross H, Proukakis C, Priestman DA, Neville DCA, Reinkensmeier G, et al. Infantile-onset symptomatic epilepsy syndrome caused by a homozygous loss-of-function mutation of GM3 synthase. Nat Genet. 2004;36: 1225–1229. doi:10.1038/ng1460

7. Boukhris A, Schule R, Loureiro JL, Lourenço CM, Mundwiller E, Gonzalez MA, et al. Alteration of Ganglioside Biosynthesis Responsible for Complex Hereditary Spastic Paraplegia. Am J Hum Genet. 2013;93: 118–123. doi:10.1016/j.ajhg.2013.05.006

8. Lee JS, Yoo Y, Lim BC, Kim KJ, Song J, Choi M, et al. GM3 synthase deficiency due to ST3GAL5 variants in two Korean female siblings: Masquerading as Rett syndrome-like phenotype. Am J Med Genet A. 2016;170: 2200–2205. doi:10.1002/ajmg.a.37773

9. Heide S, Jacquemont M-L, Cheillan D, Renouil M, Tallot M, Schwartz CE, et al. GM3 synthase deficiency in non-Amish patients. Genet Med Off J Am Coll Med Genet. 2022;24: 492–498. doi:10.1016/j.gim.2021.10.007

10. Manoochehri J, Dastgheib SA, Khamirani HJ, Mollaie M, Sharifi Z, Zoghi S, et al. A novel frameshift pathogenic variant in ST3GAL5 causing salt and pepper developmental regression syndrome (SPDRS): A case report. Hum Genome Var. 2021;8: 33. doi:10.1038/s41439-021-00164-8

11. Bowser LE, Young M, Wenger OK, Ammous Z, Brigatti KW, Carson VJ, et al. Recessive GM3 synthase deficiency: Natural history, biochemistry, and therapeutic frontier. Mol Genet Metab. 2019;126: 475–488. doi:10.1016/j.ymgme.2019.01.013

12. Inamori K-I, Inokuchi J-I. Ganglioside GM3 Synthase Deficiency in Mouse Models and Human Patients. Int J Mol Sci. 2022;23: 5368. doi:10.3390/ijms23105368

13. Indellicato R, Parini R, Domenighini R, Malagolini N, Iascone M, Gasperini S, et al. Total loss of GM3 synthase activity by a normally processed enzyme in a novel variant and in all ST3GAL5 variants reported to cause a distinct congenital disorder of glycosylation. Glycobiology. 2019;29: 229–241. doi:10.1093/glycob/cwy112

14. Giacomozzi S, Bonan L, La Morgia C, Carbonelli M, Santucci M, Isidori F, et al. Expanding the Clinical Spectrum of SPG26: A Case Report and Review of B4GALNT1-Associated Hereditary Spastic Paraplegia. Mov Disord Clin Pract. 2025;12: 1425–1428. doi:10.1002/mdc3.70062

15. Inamori K-I, Nakamura K, Shishido F, Hsu J-C, Nagafuku M, Nitta T, et al. Functional evaluation of novel variants of B4GALNT1 in a patient with hereditary spastic paraplegia and the general population. Front Neurosci. 2024;18: 1437668. doi:10.3389/fnins.2024.1437668

16. Alecu JE, Ohmi Y, Bhuiyan RH, Inamori K-I, Nitta T, Saffari A, et al. Functional validation of novel variants in B4GALNT1 associated with early-onset complex hereditary spastic paraplegia with impaired ganglioside synthesis. Am J Med Genet A. 2022;188: 2590–2598. doi:10.1002/ajmg.a.62880

17. Welland JWJ, Barrow HG, Stansfeld PJ, Deane JE. Conformational dynamics and membrane insertion mechanism of B4GALNT1 in ganglioside synthesis. Nat Commun. 2025;16: 5442. doi:10.1038/s41467-025-60593-9

18. Bharathi SS, Zhang BB, Paul E, Zhang Y, Schmidt AV, Fowler B, et al. GM3 synthase deficiency increases brain glucose metabolism in mice. Mol Genet Metab. 2022;137: 342–348. doi:10.1016/j.ymgme.2022.10.006

19. Yoshikawa M, Go S, Takasaki K, Kakazu Y, Ohashi M, Nagafuku M, et al. Mice lacking ganglioside GM3 synthase exhibit complete hearing loss due to selective degeneration of the organ of Corti. Proc Natl Acad Sci U S A. 2009;106: 9483–9488. doi:10.1073/pnas.0903279106

20. Chowdhury S, Kumar R, Zepeda E, DeFrees S, Ledeen R. Synthetic GM1 improves motor and memory dysfunctions in mice with monoallelic or biallelic disruption of GM3 synthase. FEBS Open Bio. 2023;13: 1651–1657. doi:10.1002/2211-5463.13669

21. Sheikh KA, Sun J, Liu Y, Kawai H, Crawford TO, Proia RL, et al. Mice lacking complex gangliosides develop Wallerian degeneration and myelination defects. Proc Natl Acad Sci U S A. 1999;96: 7532–7537. doi:10.1073/pnas.96.13.7532

22. Chiavegatto S, Sun J, Nelson RJ, Schnaar RL. A functional role for complex gangliosides: motor deficits in GM2/GD2 synthase knockout mice. Exp Neurol. 2000;166: 227–234. doi:10.1006/exnr.2000.7504

23. Sango K, Yamanaka S, Hoffmann A, Okuda Y, Grinberg A, Westphal H, et al. Mouse models of Tay-Sachs and Sandhoff diseases differ in neurologic phenotype and ganglioside metabolism. Nat Genet. 1995;11: 170–176. doi:10.1038/ng1095-170

24. Boccuto L, Aoki K, Flanagan-Steet H, Chen C-F, Fan X, Bartel F, et al. A mutation in a ganglioside biosynthetic enzyme, ST3GAL5, results in salt & pepper syndrome, a neurocutaneous disorder with altered glycolipid and glycoprotein glycosylation. Hum Mol Genet. 2014;23: 418–433. doi:10.1093/hmg/ddt434

25. Chiricozzi E, Lunghi G, Valsecchi M, Carsana EV, Bassi R, Di Biase E, et al. Metabolic and Structural Consequences of GM3 Synthase Deficiency: Insights from an HEK293-T Knockout Model. Biomedicines. 2025;13: 843. doi:10.3390/biomedicines13040843

26. Fernandopulle MS, Prestil R, Grunseich C, Wang C, Gan L, Ward ME. Transcription Factor-Mediated Differentiation of Human iPSCs into Neurons. Curr Protoc Cell Biol. 2018;79: e51. doi:10.1002/cpcb.51

27. Tian R, Gachechiladze MA, Ludwig CH, Laurie MT, Hong JY, Nathaniel D, et al. CRISPR Interference-Based Platform for Multimodal Genetic Screens in Human iPSC-Derived Neurons. Neuron. 2019;104: 239-255.e12. doi:10.1016/j.neuron.2019.07.014

28. Nicholson AS, Priestman DA, Antrobus R, Williamson JC, Bush R, McKie SJ, et al. Plasma Membrane Remodeling in GM2 Gangliosidoses Drives Synaptic Dysfunction. PLOS Biol. 2025;23: e3003265.

29. Rodger C, Flex E, Allison RJ, Sanchis-Juan A, Hasenahuer MA, Cecchetti S, et al. De Novo VPS4A Mutations Cause Multisystem Disease with Abnormal Neurodevelopment. Am J Hum Genet. 2020;107: 1129–1148. doi:10.1016/j.ajhg.2020.10.012

30. Hasan S, Fernandopulle MS, Humble SW, Frankenfield AM, Li H, Prestil R, et al. Multi-modal proteomic characterization of lysosomal function and proteostasis in progranulin-deficient neurons. Mol Neurodegener. 2023;18: 87. doi:10.1186/s13024-023-00673-w

31. Müthing J. High-resolution thin-layer chromatography of gangliosides. J Chromatogr A. 1996;720: 3–25. doi:10.1016/0021-9673(95)00499-8

32. Hořejší K, Kolářová D, Jirásko R, Holčapek M. Recent advances, challenges, and future directions in the mass spectrometry analysis of glycosphingolipids in biological samples. TrAC Trends Anal Chem. 2024;178: 117827. doi:10.1016/j.trac.2024.117827

33. Wing DR, Garner B, Hunnam V, Reinkensmeier G, Andersson U, Harvey DJ, et al. High-Performance Liquid Chromatography Analysis of Ganglioside Carbohydrates at the Picomole Level after Ceramide Glycanase Digestion and Fluorescent Labeling with 2-Aminobenzamide. Anal Biochem. 2001;298: 207–217. doi:10.1006/abio.2001.5393

34. Neville DCA, Coquard V, Priestman DA, te Vruchte DJM, Sillence DJ, Dwek RA, et al. Analysis of fluorescently labeled glycosphingolipid-derived oligosaccharides following ceramide glycanase digestion and anthranilic acid labeling. Anal Biochem. 2004;331: 275–282. doi:10.1016/j.ab.2004.03.051

35. Priestman DA, Weng Y, Sabir M, Bush R, Wallom K-L, Fernández-Suárez M, et al. Analysis of glycosphingolipids from cell lines. 2024 [cited 17 Mar 2026]. Available: https://www.protocols.io/view/analysis-of-glycosphingolipids-from-cell-lines-x54v9pn14g3e/v1

36. Russo D, Capolupo L, Loomba JS, Sticco L, D'Angelo G. Glycosphingolipid metabolism in cell fate specification. J Cell Sci. 2018;131: jcs219204. doi:10.1242/jcs.219204

37. Shevinsky LH, Knowles BB, Damjanov I, Solter D. Monoclonal antibody to murine embryos defines a stage-specific embryonic antigen expressed on mouse embryos and human teratocarcinoma cells. Cell. 1982;30: 697–705. doi:10.1016/0092-8674(82)90274-4

38. Kojima Y, Fukumoto S, Furukawa K, Okajima T, Wiels J, Yokoyama K, et al. Molecular cloning of globotriaosylceramide/CD77 synthase, a glycosyltransferase that initiates the synthesis of globo series glycosphingolipids. J Biol Chem. 2000;275: 15152–15156. doi:10.1074/jbc.M909620199

39. McKie SJ, Nicholson AS, Smith E, Fawke S, Caroe ER, Williamson JC, et al. Altered plasma membrane abundance of the sulfatide-binding protein NF155 links glycosphingolipid imbalances to demyelination. Proc Natl Acad Sci U S A. 2023;120: e2218823120. doi:10.1073/pnas.2218823120

40. Crunelli V, David F, Morais TP, Lorincz ML. HCN channels and absence seizures. Neurobiol Dis. 2023;181: 106107. doi:10.1016/j.nbd.2023.106107

41. He C, Chen F, Li B, Hu Z. Neurophysiology of HCN channels: From cellular functions to multiple regulations. Prog Neurobiol. 2014;112: 1–23. doi:10.1016/j.pneurobio.2013.10.001

42. Byczkowicz N, Eshra A, Montanaro J, Trevisiol A, Hirrlinger J, Kole MH, et al. HCN channel-mediated neuromodulation can control action potential velocity and fidelity in central axons. Raman IM, Calabrese RL, Golding N, editors. eLife. 2019;8: e42766. doi:10.7554/eLife.42766

43. Schwarz JR, Freitag S, Pechmann Y, Hermans-Borgmeyer I, Wagner W, Hornig S, et al. Purkinje cell hyperexcitability and depressive-like behavior in mice lacking erg3 (ether-à-go-go-related gene) K+ channel subunits. Sci Adv. 2024;10: eadn6836. doi:10.1126/sciadv.adn6836

44. Tsai M-H, Lo C-H, Liu Y-X, Wu S-N, Kuo C-Y, Liu Y-H, et al. De novo missense variants of KCNA3, KCNA4, and KCNA6 cause early onset developmental epileptic encephalopathy. Hum Mol Genet. 2025;34: 1392–1404. doi:10.1093/hmg/ddaf090

45. Davies PA, Pistis M, Hanna MC, Peters JA, Lambert JJ, Hales TG, et al. The 5-HT3B subunit is a major determinant of serotonin-receptor function. Nature. 1999;397: 359–363. doi:10.1038/16941

46. Okkenhaug H, Weylandt K-H, Carmena D, Wells DJ, Higgins CF, Sardini A. The human ClC-4 protein, a member of the CLC chloride channel/transporter family, is localized to the endoplasmic reticulum by its N-terminus. FASEB J Off Publ Fed Am Soc Exp Biol. 2006;20: 2390–2392. doi:10.1096/fj.05-5588fje

47. He H, Guzman RE, Cao D, Sierra-Marquez J, Yin F, Fahlke C, et al. The molecular and phenotypic spectrum of CLCN4-related epilepsy. Epilepsia. 2021;62: 1401–1415. doi:10.1111/epi.16906

48. Houdayer C, Phillips AM, Chabbert M, Bourreau J, Maroofian R, Houlden H, et al. HCN2-Associated Neurodevelopmental Disorders: Data from Patients and Xenopus Cell Models. Ann Neurol. 2025;98: 573–589. doi:10.1002/ana.27277

49. DiFrancesco JC, Ragona F, Murano C, Frosio A, Melgari D, Binda A, et al. A novel de novo HCN2 loss-of-function variant causing developmental and epileptic encephalopathy treated with a ketogenic diet. Epilepsia. 2023;64: e222–e228. doi:10.1111/epi.17777

50. Soldovieri MV, Ambrosino P, Mosca I, Servettini I, Pietrunti F, Belperio G, et al. De novo variants in KCNA3 cause developmental and epileptic encephalopathy. Ann Neurol. 2024;95: 365–376. doi:10.1002/ana.26826

51. Wu F, Ji X, Shen M, Cheng P, Feng S, Gao Y, et al. Whole exome sequencing identifies KCNH7 variants associated with epilepsy in children. Genes Dis. 2025;12: 101322. doi:10.1016/j.gendis.2024.101322

52. Kim J, Park D, Seo N-Y, Yoon T-H, Kim GH, Lee S-H, et al. LRRTM3 regulates activity-dependent synchronization of synapse properties in topographically connected hippocampal neural circuits. Proc Natl Acad Sci. 2022;119: e2110196119. doi:10.1073/pnas.2110196119

53. Zhang R, Jiang H, Liu Y, He G. Structure, function, and pathology of Neurexin-3. Genes Dis. 2023;10: 1908–1919. doi:10.1016/j.gendis.2022.04.008

54. Yamagata A, Goto-Ito S, Sato Y, Shiroshima T, Maeda A, Watanabe M, et al. Structural insights into modulation and selectivity of transsynaptic neurexin–LRRTM interaction. Nat Commun. 2018;9: 3964. doi:10.1038/s41467-018-06333-8

55. Um JW, Choi T-Y, Kang H, Cho YS, Choii G, Uvarov P, et al. LRRTM3 Regulates Excitatory Synapse Development through Alternative Splicing and Neurexin Binding. Cell Rep. 2016;14: 808–822. doi:10.1016/j.celrep.2015.12.081

56. Inamori K-I, Ito H, Tamura Y, Nitta T, Yang X, Nihei W, et al. Deficient ganglioside synthesis restores responsiveness to leptin and melanocortin signaling in obese KKAy mice. J Lipid Res. 2018;59: 1472–1481. doi:10.1194/jlr.M085753

57. Yamashita T, Hashiramoto A, Haluzik M, Mizukami H, Beck S, Norton A, et al. Enhanced insulin sensitivity in mice lacking ganglioside GM3. Proc Natl Acad Sci U S A. 2003;100: 3445–3449. doi:10.1073/pnas.0635898100

58. Yamashita T, Wu Y-P, Sandhoff R, Werth N, Mizukami H, Ellis JM, et al. Interruption of ganglioside synthesis produces central nervous system degeneration and altered axon-glial interactions. Proc Natl Acad Sci U S A. 2005;102: 2725–2730. doi:10.1073/pnas.0407785102

59. Brigande JV, Platt FM, Seyfried TN. Inhibition of Glycosphingolipid Biosynthesis Does Not Impair Growth or Morphogenesis of the Postimplantation Mouse Embryo. J Neurochem. 1998;70: 871–882. doi:10.1046/j.1471-4159.1998.70020871.x

60. Inokuchi J-I, Go S, Suzuki A, Nakagawasai O, Odaira-Satoh T, Veillon L, et al. Dietary gangliosides rescue GM3 synthase deficiency outcomes in mice accompanied by neurogenesis in the hippocampus. Front Neurosci. 2024;18: 1387221. doi:10.3389/fnins.2024.1387221

61. Fragaki K, Ait-El-Mkadem S, Chaussenot A, Gire C, Mengual R, Bonesso L, et al. Refractory epilepsy and mitochondrial dysfunction due to GM3 synthase deficiency. Eur J Hum Genet EJHG. 2013;21: 528–534. doi:10.1038/ejhg.2012.202

62. Pan B, Fromholt SE, Hess EJ, Crawford TO, Griffin JW, Sheikh KA, et al. Myelin-associated glycoprotein and complementary axonal ligands, gangliosides, mediate axon stability in the CNS and PNS: neuropathology and behavioral deficits in single- and double-null mice. Exp Neurol. 2005;195: 208–217. doi:10.1016/j.expneurol.2005.04.017

63. Takamiya K, Yamamoto A, Furukawa K, Yamashiro S, Shin M, Okada M, et al. Mice with disrupted GM2/GD2 synthase gene lack complex gangliosides but exhibit only subtle

defects in their nervous system. Proc Natl Acad Sci. 1996;93: 10662–10667. doi:10.1073/pnas.93.20.10662

64. Yao D, McGonigal R, Barrie JA, Cappell J, Cunningham ME, Meehan GR, et al. Neuronal Expression of GalNAc Transferase Is Sufficient to Prevent the Age-Related Neurodegenerative Phenotype of Complex Ganglioside-Deficient Mice. J Neurosci. 2014;34: 880–891. doi:10.1523/JNEUROSCI.3996-13.2014

65. Harlalka GV, Lehman A, Chioza B, Baple EL, Maroofian R, Cross H, et al. Mutations in B4GALNT1 (GM2 synthase) underlie a new disorder of ganglioside biosynthesis. Brain J Neurol. 2013;136: 3618–3624. doi:10.1093/brain/awt270

66. Max SR, Maclaren NK, Brady RO, Bradley RM, Rennels MB, Tanaka J, et al. GM3 (hematoside) sphingolipodystrophy. N Engl J Med. 1974;291: 929–931. doi:10.1056/NEJM197410312911802

67. Trinchera M, Parini R, Indellicato R, Domenighini R, dall'Olio F. Diseases of ganglioside biosynthesis: An expanding group of congenital disorders of glycosylation. Mol Genet Metab. 2018;124: 230–237. doi:10.1016/j.ymgme.2018.06.014

68. Kawai H, Allende ML, Wada R, Kono M, Sango K, Deng C, et al. Mice Expressing Only Monosialoganglioside GM3 Exhibit Lethal Audiogenic Seizures *. J Biol Chem. 2001;276: 6885–6888. doi:10.1074/jbc.C000847200

69. Inoue M, Fujii Y, Furukawa K, Okada M, Okumura K, Hayakawa T, et al. Refractory Skin Injury in Complex Knock-out Mice Expressing Only the GM3 Ganglioside *. J Biol Chem. 2002;277: 29881–29888. doi:10.1074/jbc.M201631200

70. Castello-Serrano I, Heberle FA, Diaz-Rohrer B, Ippolito R, Shurer CR, Lujan P, et al. Partitioning to ordered membrane domains regulates the kinetics of secretory traffic. eLife. 2024;12: RP89306. doi:10.7554/eLife.89306

71. Lorent JH, Diaz-Rohrer B, Lin X, Spring K, Gorfe AA, Levental KR, et al. Structural determinants and functional consequences of protein affinity for membrane rafts. Nat Commun. 2017;8: 1219. doi:10.1038/s41467-017-01328-3

72. Schmieder SS, Tatituri R, Anderson M, Kelly K, Lencer WI. Structural basis for acyl chain control over glycosphingolipid sorting and vesicular trafficking. Cell Rep. 2022;40: 111063. doi:10.1016/j.celrep.2022.111063

73. Diaz-Rohrer B, Levental KR, Levental I. Rafting through traffic: Membrane domains in cellular logistics. Biochim Biophys Acta. 2014;1838: 3003–3013. doi:10.1016/j.bbamem.2014.07.029

74. Svistunov VO, Ehrmann KJ, Lencer WI, Schmieder SS. Sorting of complex sphingolipids within the cellular endomembrane systems. Front Cell Dev Biol. 2024;12: 1490870. doi:10.3389/fcell.2024.1490870

75. Aguilera-Romero A, Lucena R, Sabido-Bozo S, Muñiz M. Impact of sphingolipids on protein membrane trafficking. Biochim Biophys Acta BBA - Mol Cell Biol Lipids. 2023;1868: 159334. doi:10.1016/j.bbalip.2023.159334

76. Johannes L, Shafaq-Zadah M, Dransart E, Wunder C, Leffler H. Endocytic Roles of Glycans on Proteins and Lipids. Cold Spring Harb Perspect Biol. 2024;16: a041398. doi:10.1101/cshperspect.a041398

77. Johannes L, Billet A. Glycosylation and raft endocytosis in cancer. Cancer Metastasis Rev. 2020;39: 375–396. doi:10.1007/s10555-020-09880-z

78. Johannes L, Wunder C, Shafaq-Zadah M. Glycolipids and Lectins in Endocytic Uptake Processes. J Mol Biol. 2016; S0022-2836(16)30453–3. doi:10.1016/j.jmb.2016.10.027

79. Chiu Y-P, Sun Y-C, Qiu D-C, Lin Y-H, Chen Y-Q, Kuo J-C, et al. Liquid-liquid phase separation and extracellular multivalent interactions in the tale of galectin-3. Nat Commun. 2020;11: 1229. doi:10.1038/s41467-020-15007-3

80. Mathew MP, Donaldson JG. Distinct cargo-specific response landscapes underpin the complex and nuanced role of galectin-glycan interactions in clathrin-independent endocytosis. J Biol Chem. 2018;293: 7222–7237. doi:10.1074/jbc.RA118.001802

81. Ravindran MS, Tanner LB, Wenk MR. Sialic acid linkage in glycosphingolipids is a molecular correlate for trafficking and delivery of extracellular cargo. Traffic Cph Den. 2013;14: 1182–1191. doi:10.1111/tra.12100

82. Ghorashi AC, Boucher A, Archer-Hartmann SA, Zalem D, Taherzadeh Ghahfarrokhi M, Murray NB, et al. Fucosylation of glycoproteins and glycolipids: opposing roles in cholera intoxication. Nat Chem Biol. 2025;21: 555–566. doi:10.1038/s41589-024-01748-5

83. Heim JB, Hodnik V, Heggelund JE, Anderluh G, Krengel U. Crystal structures of cholera toxin in complex with fucosylated receptors point to importance of secondary binding site. Sci Rep. 2019;9: 12243. doi:10.1038/s41598-019-48579-2

84. Flores A, Ramirez-Franco J, Desplantes R, Debreux K, Ferracci G, Wernert F, et al. Gangliosides interact with synaptotagmin to form the high-affinity receptor complex for botulinum neurotoxin B. Proc Natl Acad Sci U S A. 2019;116: 18098–18108. doi:10.1073/pnas.1908051116

85. Heggelund JE, Burschowsky D, Bjørnestad VA, Hodnik V, Anderluh G, Krengel U. High-Resolution Crystal Structures Elucidate the Molecular Basis of Cholera Blood Group Dependence. PLoS Pathog. 2016;12: e1005567. doi:10.1371/journal.ppat.1005567

86. Zhang G-L, Porter MJ, Awol AK, Orsburn BC, Canner SW, Gray JJ, et al. The Human Ganglioside Interactome in Live Cells Revealed Using Clickable Photoaffinity Ganglioside Probes. J Am Chem Soc. 2024;146: 17801–17816. doi:10.1021/jacs.4c03196

87. Kundu S, Rohokale R, Lin C, Chen S, Biswas S, Guo Z. Bifunctional glycosphingolipid (GSL) probes to investigate GSL-interacting proteins in cell membranes. J Lipid Res. 2024;65. doi:10.1016/j.jlr.2024.100570

88. Favell JW, Bui DT, Li J, Han L, Kitova EN, Schmidt EN, et al. Elusive Protein-Glycosphingolipid Interactions Revealed by Membrane Anchor-Assisted Native Mass Spectrometry. J Am Chem Soc. 2024;146: 21700–21709. doi:10.1021/jacs.4c05805

89. Russo D, Parashuraman S, D'Angelo G. Glycosphingolipid–Protein Interaction in Signal Transduction. Int J Mol Sci. 2016;17: 1732. doi:10.3390/ijms17101732

90. Coskun Ü, Grzybek M, Drechsel D, Simons K. Regulation of human EGF receptor by lipids. Proc Natl Acad Sci U S A. 2011;108: 9044–9048. doi:10.1073/pnas.1105666108

91. Song W, Yen H-Y, Robinson CV, Sansom MSP. State-dependent Lipid Interactions with the A2a Receptor Revealed by MD Simulations Using *In Vivo*-Mimetic Membranes. Structure. 2019;27: 392-403.e3. doi:10.1016/j.str.2018.10.024

92. Yakel JL, Jackson MB. 5-HT3 receptors mediate rapid responses in cultured hippocampus and a clonal cell line. Neuron. 1988;1: 615–621. doi:10.1016/0896-6273(88)90111-0

93. Mishra P, Narayanan R. The enigmatic HCN channels: A cellular neurophysiology perspective. Proteins. 2025;93: 72–92. doi:10.1002/prot.26643

94. Li M, Maljevic S, Phillips AM, Petrovski S, Hildebrand MS, Burgess R, et al. Gain-of-function HCN2 variants in genetic epilepsy. Hum Mutat. 2018;39: 202–209. doi:10.1002/humu.23357

95. Wu Z, Chen G, Qiu C, Yan X, Xu L, Jiang S, et al. Structural basis for the ligand recognition and G protein subtype selectivity of kisspeptin receptor. Sci Adv. 2024;10: eadn7771. doi:10.1126/sciadv.adn7771

96. Yan C, Zeng T, Lee K, Nobis M, Loh K, Gou L, et al. Peripheral-specific Y1 receptor antagonism increases thermogenesis and protects against diet-induced obesity. Nat Commun. 2021;12: 2622. doi:10.1038/s41467-021-22925-3

97. Porro A, Saponaro A, Castelli R, Introini B, Hafez Alkotob A, Ranjbari G, et al. A high affinity switch for cAMP in the HCN pacemaker channels. Nat Commun. 2024;15: 843. doi:10.1038/s41467-024-45136-y

98. Kalkan ÖF, Şahin Z, Aktaş O, Yildirim A, Aydin Abidin S, Özyaşar AF, et al. Central administration of p234, kisspeptin antagonist, but not kisspeptin-10, reduces the power of epileptiform activity and slow EEG waves in male rats. Neurol Res. 2025;47: 139–146. doi:10.1080/01616412.2025.2456293

99. Cattaneo S, Verlengia G, Marino P, Simonato M, Bettegazzi B. NPY and Gene Therapy for Epilepsy: How, When,... and Y. Front Mol Neurosci. 2020;13: 608001. doi:10.3389/fnmol.2020.608001

100. Watanabe S, Lei M, Nakagawa E, Takeshita E, Inamori K-I, Shishido F, et al. Neurological insights on two siblings with GM3 synthase deficiency due to novel compound heterozygous ST3GAL5 variants. Brain Dev. 2023;45: 270–277. doi:10.1016/j.braindev.2023.01.002

101. Reitz C, Conrad C, Roszkowski K, Rogers RS, Mayeux R. Effect of genetic variation in LRRTM3 on risk of Alzheimer disease. Arch Neurol. 2012;69: 894–900. doi:10.1001/archneurol.2011.2463

102. Bonham LW, Karch CM, Fan CC, Tan C, Geier EG, Wang Y, et al. CXCR4 involvement in neurodegenerative diseases. Transl Psychiatry. 2018;8: 73. doi:10.1038/s41398-017-0049-7

103. Zhang X, Zhang Y, Zhang T, Wang J, Liu C, Shang Q, et al. HCN2 deficiency correlates with memory deficits and hyperexcitability of dCA1 pyramidal neurons in Alzheimer's disease. Alzheimers Res Ther. 2025;17: 55. doi:10.1186/s13195-025-01704-y

104. Hicks DA, Nalivaeva NN, Turner AJ. Lipid rafts and Alzheimer's disease: protein-lipid interactions and perturbation of signaling. Front Physiol. 2012;3: 189. doi:10.3389/fphys.2012.00189

105. Kubo S, Hatano T, Hattori N. Lipid rafts involvement in the pathogenesis of Parkinson's disease. Front Biosci Landmark Ed. 2015;20: 263–279. doi:10.2741/4308

106. Weesner JA, Annunziata I, van de Vlekkert D, d'Azzo A. Glycosphingolipids within membrane contact sites influence their function as signaling hubs in neurodegenerative diseases. FEBS Open Bio. 2023;13: 1587–1600. doi:10.1002/2211-5463.13605

107. Platt FM, d'Azzo A, Davidson BL, Neufeld EF, Tifft CJ. Lysosomal storage diseases. Nat Rev Dis Primer. 2018;4: 27. doi:10.1038/s41572-018-0025-4

108. Platt FM. Sphingolipid lysosomal storage disorders. Nature. 2014;510: 68–75. doi:10.1038/nature13476

109. Stringer BW, Day BW, D'Souza RCJ, Jamieson PR, Ensbey KS, Bruce ZC, et al. A reference collection of patient-derived cell line and xenograft models of proneural, classical and mesenchymal glioblastoma. Sci Rep. 2019;9: 4902. doi:10.1038/s41598-019-41277-z

110. Livak KJ, Schmittgen TD. Analysis of relative gene expression data using real-time quantitative PCR and the 2(-Delta Delta C(T)) Method. Methods San Diego Calif. 2001;25: 402–408. doi:10.1006/meth.2001.1262

111. Nightingale K, Lin K-M, Ravenhill BJ, Davies C, Nobre L, Fielding CA, et al. High-Definition Analysis of Host Protein Stability during Human Cytomegalovirus Infection Reveals Antiviral Factors and Viral Evasion Mechanisms. Cell Host Microbe. 2018;24: 447-460.e11. doi:10.1016/j.chom.2018.07.011

112. McAlister GC, Nusinow DP, Jedrychowski MP, Wühr M, Huttlin EL, Erickson BK, et al. MultiNotch MS3 enables accurate, sensitive, and multiplexed detection of differential expression across cancer cell line proteomes. Anal Chem. 2014;86: 7150–7158. doi:10.1021/ac502040v

113. Demichev V, Messner CB, Vernardis SI, Lilley KS, Ralser M. DIA-NN: neural networks and interference correction enable deep proteome coverage in high throughput. Nat Methods. 2020;17: 41–44. doi:10.1038/s41592-019-0638-x

114. Tyanova S, Temu T, Sinitcyn P, Carlson A, Hein MY, Geiger T, et al. The Perseus computational platform for comprehensive analysis of (prote)omics data. Nat Methods. 2016;13: 731–740. doi:10.1038/nmeth.3901

FIGURES AND FIGURE LEGENDS

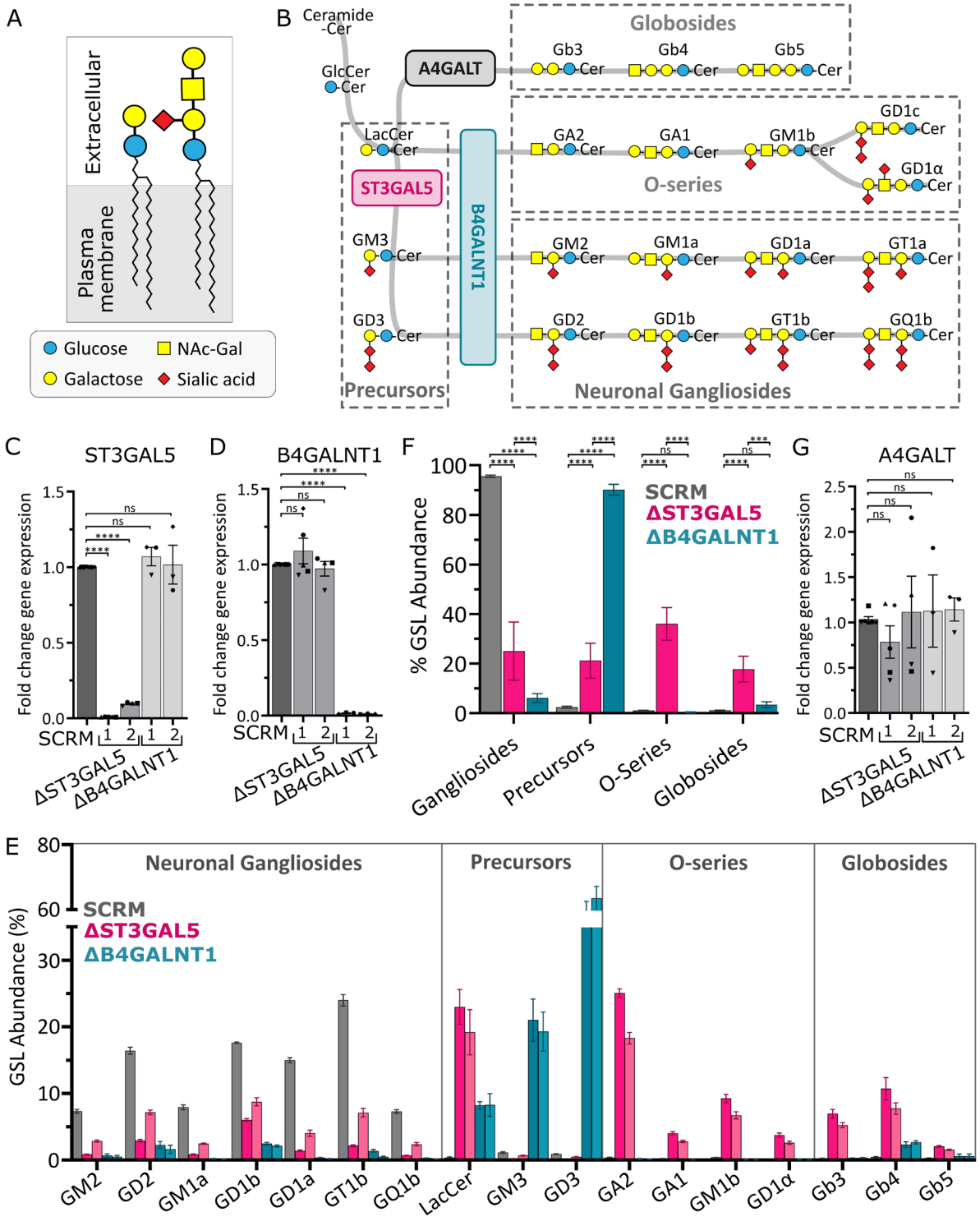

Figure 1: ΔST3GAL5 and ΔB4GALNT1 i3 neurons have severe and contrasting changes to their GSL composition. (A) Simplified diagram of glycosphingolipid (GSL) structure with a membrane embedded ceramide tail and extracellular glycan head groups. (B) Schematic of GSL synthesis with lipid series (dashed boxes) and select enzymes (solid boxes) labelled. qPCR of (C) ST3GAL5,

(D) B4GALNT1 and (G) A4GALT gene expression in i3N at 28 dpi. Fold change relative to SCRM controls are shown for each cell line. The mean ± SEM is shown for N = 3-6 biological replicates (squares, triangles, circles, diamonds, hexagons) carried out in technical triplicate. Statistical significance was calculated using one-way ANOVA with Dunnett's multiple comparisons testing, ****$p \leq 0.0001$. (E) Quantification of whole cell GSL composition of i3Ns at 28 dpi by glycan profiling. The two shades of pink and blue reflect the two guides targeting each gene, GSL quantitation is displayed as percentage of total GSL abundance, mean ± SEM for N = 3-6 biological replicates. For clarity statistical significance for individual pairwise GSLs comparisons are provided in Supplementary Figure S3. (F) Data from (E) grouped by lipid series into gangliosides (GM2, GD2, GM1a, GD1b, GD1a, GT1b, GQ1b), precursors (LacCer, GM3, GD3, GD1α), O-series (GA2, GA1, GM1b) and globosides (Gb3, Gb4, Gb5). Mean ± SEM. Significance calculated using two-way ANOVA with Dunnett's multiple comparisons testing, ****$p \leq 0.0001$, ***$p \leq 0.001$, ns not significant.

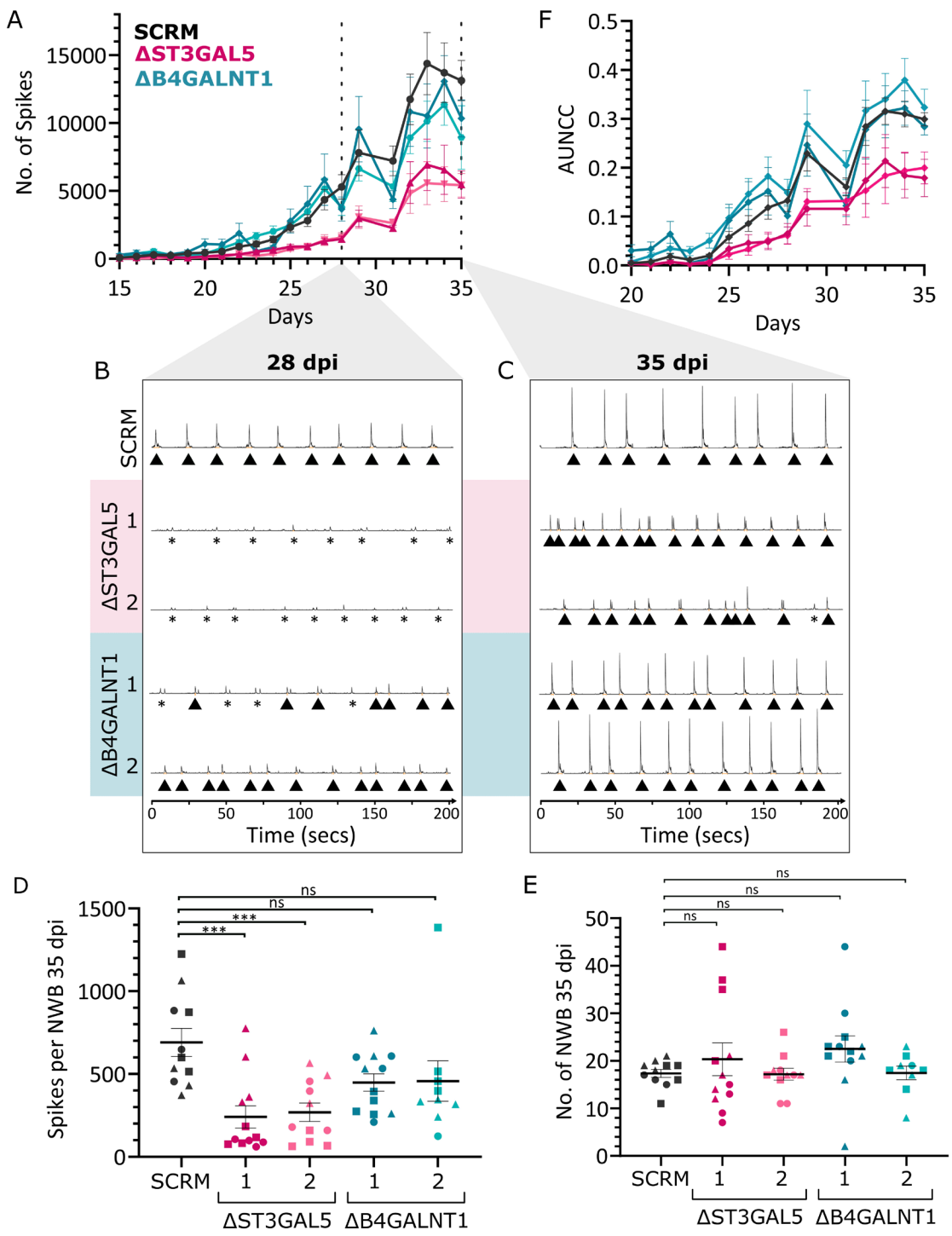

Figure 2: ΔST3GAL5 but not ΔB4GALNT1 neurons display severely disrupted electrical signalling. SCRM, ΔST3GAL5 and ΔB4GALNT1 neurons were cultured in 24 well multi-electrode array (MEA) plates and recordings were taken throughout differentiation. (A) Time courses monitoring number of spikes are shown for all cell lines with dashed lines indicating 28 and 35 dpi. The two shades of pink and blue reflect the two guides targeting each gene, Mean and SEM

are shown for 9-12 wells measured per condition over N=3 biological replicates. Representative frequency histograms of spikes at 28 dpi (B) and 35 dpi (C). Triangles indicate network burst events. Asterisks represent synchronous firing events that don't meet the threshold required to be a network burst. Spikes per NWB (D) and number of NWB (E) at 35 dpi for all cell lines. Mean ± SEM are shown for 9-12 wells measured per condition across N=3 biological replicates (circle, square, triangle). Significance calculated using one-way ANOVA with Dunnett's multiple comparisons testing against SCRM, ***$p \leq 0.001$, ns not significant. (F) Area under normalized cross-correlation (AUNCC) over time. Mean +/- SEM is shown for 9-12 wells measured per condition across N=3 biological replicates.

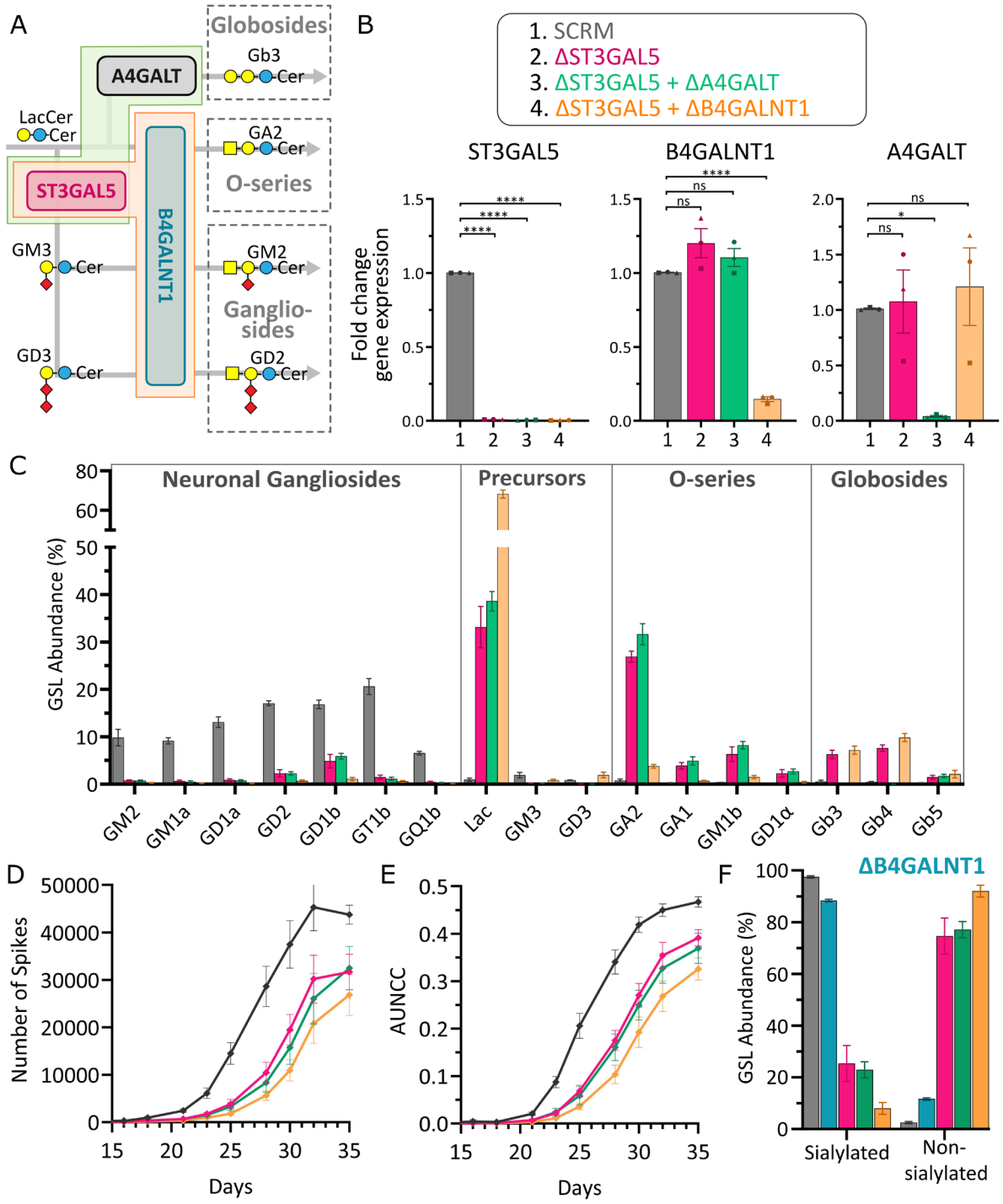

Figure 3: Accumulation of globosides or O-series lipids is not responsible for the disrupted electrical signalling in ΔST3GAL5 neurons. (A) Truncated schematic of GSL synthesis, highlighting the generation of double knock-down cell lines ΔST3GAL5+ΔA4GALT (green) and ΔST3GAL5+ΔB4GALNT1 (orange). Lipid series (dashed lines) and selected enzymes (solid lines) are boxed. (B) qPCR of i3N at 28 dpi, shown as fold change against SCRM. Mean ± SEM is shown for N=3 biological replicates (circle, square, triangle). Significance was calculated using one-way ANOVA with Dunnett's multiple comparisons testing against SCRM, ****$p \leq 0.0001$, * $p \leq 0.05$, ns

not significant. (C) Quantification of whole cell GSL composition of i3Ns at 28 dpi by glycan profiling. GSL quantitation is displayed as percentage of total GSL abundance, mean ± SEM for N = 3 biological replicates. For clarity statistical significance for individual pairwise GSLs comparisons are provided in Supplementary Figure S8. Time course of MEA data showing (D) number of spikes and (E) area under normalized cross-correlation (AUNCC) over time. Mean ± SEM are shown for 9-12 wells measured per condition across N=3 biological replicates. (F) Data from (Fig. 1E and 3C) grouped by sialic acid content into sialyated (GM2, GD2, GM1a, GD1b, GD1a, GT1b, GQ1b, GM3, GD3, GM1b, GD1α) or non-sialyated (LacCer, GA2, GA1, Gb3, Gb4, Gb5).

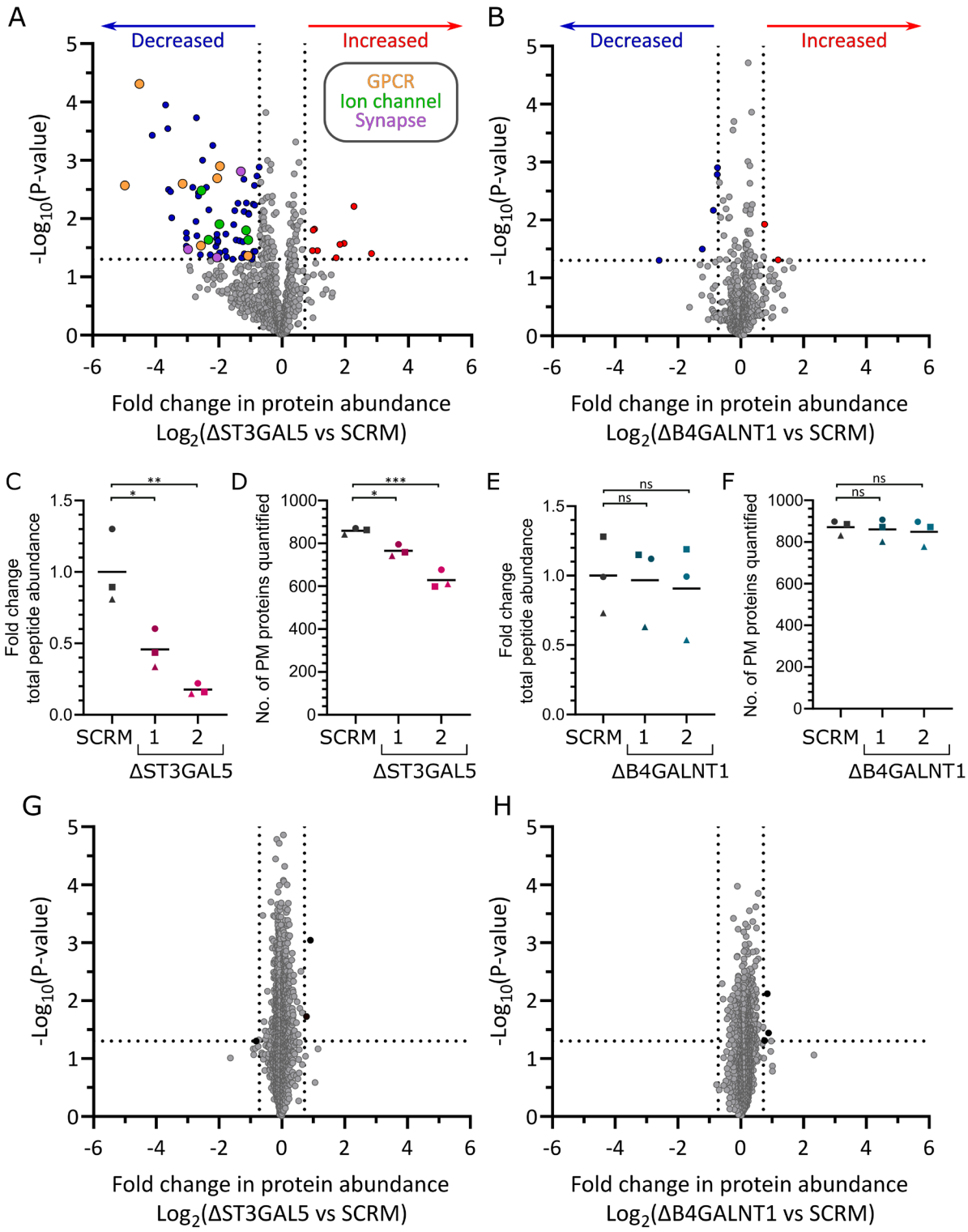

Figure 4. Loss of sialylated GSLs changes the neuronal cell surface proteome. Quantitative mass spectrometry following enrichment of PM proteins from ΔST3GAL5 and ΔB4GALNT1 neurons compared with the SCRM control. Plasma membrane proteomics data are displayed as volcano plots of ΔST3GAL5 (A) and ΔB4GALNT1 (B) neurons compared to SCRM neurons and shown with average fold change (x-axis) across three biological replicates and significance (y-

axis, two-sided t test) across the three replicates. Protein targets are coloured based on reduced (blue) or increased (red) abundance with some specific protein classes labelled including GPCRs (orange), ion channels (green) and synaptic proteins (purple). (C) Total peptide abundance of ΔST3GAL5 samples, presented as fold change against SCRM . (D) Number of quantified plasma membrane proteins in ΔST3GAL5 samples. Equivalent analyses are shown for ΔB4GALNT1 samples in (E) and (F). Significance was calculated using one-way ANOVA with Dunnett's multiple comparisons testing against SCRM, ***$p \leq 0.001$, **$p \leq 0.01$ * $p \leq 0.05$, ns not significant. Volcano plots for whole cell proteomics data for ΔST3GAL5 (G) and ΔB4GALNT1 (H) neurons compared to SCRM neurons. Data displayed as for panels (A) and (B).